Challenge Journal of

CONCRETE RESEARCH LETTERS

Vol.15 No.2 (2024)

acoustic emission aerated concrete artificial neural network compressive strength corrosion cracking ductility durability energy absorption ferrocement flexural strength fly ash fracture mechanics mechanical properties mortar nanoparticle reinforced concrete self- compacting concrete steam curing strengthening superplasticizer tensile strength workability waste disposal water a tion

ISSN 2548-0928

TULPAR
ACADEMIC PUBLISHING

Challenge Journal of Concrete Research Letters

E-mail: *cjcrl@challengejournal.com*

Web page: *cjcrl.challengejournal.com*

Tulpar Academic Publishing
www.tulparpublishing.com

Challenge Journal of Concrete Research Letters

CONTENTS

Research Articles

TULPAR ACADEMIC PUBLISHING

Challenge Journal of Concrete Research Letters

Research Article

The impact of openings on ferrocement I-beams: a study on metallic and non-metallic mesh reinforcement

Ghada Mousa Hekal [a,*], Ayman Magdy Moawad Elshaboury [b], Yousry B. I. Shaheen [a]

[a] *Department of Civil Engineering, Menoufia University, Shebin ElKoum, Menofia, Egypt*
[b] *Department of Construction, Higher Institute of Engineering and Technology, Beheira, Egypt*

ABSTRACT

The primary objective of this investigation is to assess the influence of openings on the structural performance of ferrocement I-beams, incorporating diverse metallic and non-metallic mesh reinforcements. Sixteen beams underwent testing utilizing a four-point loading system until failure, categorized into four groups based on the type of mesh reinforcement. Each group comprised a control I-beam without openings and three additional beams featuring one, two, and three openings, respectively. To ensure consistent reinforcement weight, the four groups were reinforced with three layers of welded steel meshes, two layers of expanded metal meshes, two layers of Tensar meshes, and eight layers of Gavazzi meshes. Comparative analysis of the experimental outcomes was conducted with finite element models utilizing Abaqus. Therefore, there was good agreement between the experimental and numerical results. The findings showed that beams with no openings, one, and two openings reinforced with Gavazzi meshes had the highest ultimate load compared to other tested beams, while beams with three openings, those reinforced with expanded metal meshes had the greatest ultimate loads. Placing three openings in beams, with dimensions of 100×50 mm (two of these openings are approximately 10 cm apart from each edge while the third opening is located at mid-span), reduced the load-to-weight ratio by about 20.7%, 12.9%, 8.2%, and 23.8% for welded beams, expanded beams, Tensar beams, and Gavazzi beams, respectively, compared to the beams with no openings.

ARTICLE INFO

Article history:
Received 14 September 2023
Revised 7 November 2023
Accepted 28 November 2023

Keywords:
Ferrocement
I-beams
Openings
Metallic meshes
Non-metallic meshes

1. Introduction

Ferrocement, a composite material reinforced with wire meshes, has gained attention due to its strength, serviceability, and durability as mentioned in ACI 549R (1997) and ACI 5492R (2004). This material consists of a mortar matrix with multiple layers of steel mesh reinforcement embedded within it (Shaheen et al. 2023a). It can be formed into various shapes using machinery, making it cost-effective and versatile. Ferrocement is durable, lightweight, fire-resistant, and environmentally stable as stated in a previous study conducted by Naaman (2000). Suresh (2004), and Austriaco (2006) argued that ferrocement consistent distribution of reinforcing wire meshes has made it an attractive option for pre-fabrication and construction development. The mesh can be produced from metallic or other appropriate materials (Shaheen et al. 2022a).

Several studies conducted by different authors such as Ankit et al. (2017), Shaheen et al. (2016, 2020, 2021, 2023b), Rameshkumar et al. (2022), Salman et al. (2018), Shaaban et al. (2018), Sumadi and Ramli (2008), International Ferrocement Society (2001), investigated the mechanical properties of ferrocement, including its compressive and flexural strength, as well as ductility behavior. Acma and Mariano (2014) examined ferrocement I-beams reinforced with two to six welded wire meshes and found that while the flexural strength was

* *Corresponding author*. Tel.: +02-010-698-560-09 ; E-mail address: gahda.mousa@sh-eng.menofia.edu.eg (G. M. Hekal)
ISSN: 2548-0928 / DOI: https://doi.org/10.20528/cjcrl.2024.02.001

satisfactory, the beams did not exhibit the required ductility behavior of reinforced concrete beams. Acma et al. (2015) conducted another study on ferrocement I-beams, using eight layers of welded wire mesh to reinforce C-beams. They found that the load increased with an increase in the number of welded wire mesh reinforcement layers in the flange area.

ChandraSekharRao et al. (2012) conducted an investigation on the behavior and durability of cored precast ferrocement beams with box section. They cast and tested eight box beams under a four-point bending setup, with the number of wire mesh layers as a variable parameter. The study found that the reduction in flexural strength due to vacancies was smaller than the reduction in weight, and the post-ductility increased by increasing the layer number, leading to an improvement in moment-curvature response of the cored specimens under flexural loading.

Shaheen et al. (2022b) conducted an experimental investigation on ferrocement I-beams featuring various metallic and non-metallic mesh reinforcements. 8 beams were cast, cured, and subjected to testing using a four-point bending system, with the beams categorized into two groups depending on the type of reinforcement employed. The beams reinforced with welded steel mesh exhibited superior ultimate loads, deflection, ductility ratio, and energy absorption in comparison to those reinforced with Tensar mesh. The introduction of three openings to 100×50 mm beams resulted in a reduction of the load-to-weight ratio by 20.7% and 8.2% for welded steel mesh-reinforced and Tensar mesh-reinforced beams, respectively.

This study aims to build upon previous research carried out by Shaheen et al. (2022b) by conducting a more comprehensive experimental program on ferrocement I-beams with openings, using various types of meshes for reinforcement. Ferrocement I-beams exhibit versatility in construction engineering with potential applications spanning various domains. Their high strength-to-weight ratio makes them suitable for small to medium-span bridges, marine structures like docks and piers, and building elements such as floors and roofs. Additionally, ferrocement I-beams can be employed in retaining walls, precast elements for controlled manufacturing conditions, water tanks due to their crack resistance, and infrastructure rehabilitation projects. Their lightweight nature makes them advantageous in seismic-prone regions and agricultural structures, while their corrosion resistance deems them fit for pipeline support structures. The goal is to provide further insight into the behavior of ferrocement I-beams with openings. Additionally, a finite element analysis will be conducted on all tested beams to gain a deeper understanding of their behavior. Hoping that this research will be a valuable addition to the existing literature on ferrocement and its applications.

2. Experimental Program

The authors aimed to expand on their previous research (Shaheen et al. 2022b) by conducting a more extensive experimental program, using additional ferrocement I-beams reinforced with various types of metal and non-metal meshes. The previous research referred to in this paper utilized eight ferrocement I-beams, which were divided into two groups based on the type of reinforcing mesh used, as listed in Table 1. In this study, an additional eight beams reinforced were added to the current study. These new beams were also categorized into two sets based on the type of the used reinforcing, as described in Table 1.

Table 1. Details of the tested beams (Shaheen et al. 2022b).

Group No.	Code of the beam	Meshes used	No. of openings	Volume fraction %
A	W0 control	Welded steel mesh arranged in triple layers	-	4.4
	W1		1	
	W2		2	
	W3		3	
B	T0 control	double layers of Tensar mesh (Type SS40)	-	1.3
	T1		1	
	T2		2	
	T3		3	
C	E0 control	double layers of expanded metal mesh	-	1.0
	E1		1	
	E2		2	
	E3		3	
D	G0 control	Eight-layer Gavazzi mesh (Type 0133-A)	-	4.6
	G1		1	
	G2		2	
	G3		3	

The formulation of the mortar mix in this study followed the same procedure as outlined in the prior investigation conducted by Shaheen et al. (2022b). The mortar mix included Blast furnace Cement, sand, silica fume, fly ash, water, Polypropylene mesh e300, and superplasticizer. Silica fume was used in conjunction with fly ash to achieve better strength with less cement, as demonstrated by Pathak (2020). Similarly, Safiuddin and Zain (2005) concluded that fly ash and silica fume together improved the fresh and hardened properties of concrete. Silica fume improved the permeability of concrete, while fly ash improved its strength over time. As shown in Fig. 1, Group C was reinforced with expanded metal mesh, while group D was reinforced with Gavazzi mesh. Tables 2 and 3 provide the technical specifications and mechanical properties of the expanded metal and Gavazzi meshes, respectively according to the manufacturer.

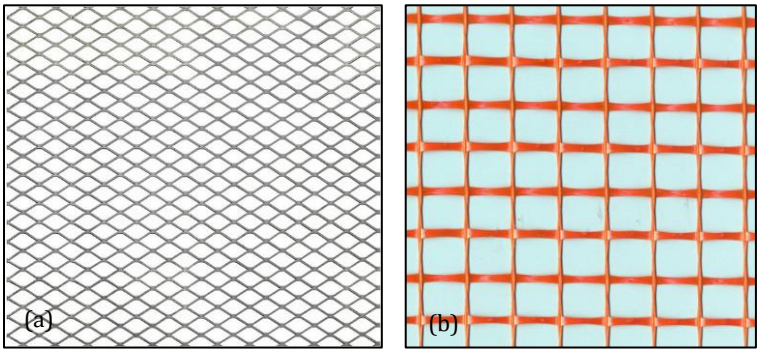

Fig. 1. The meshes applied to groups C and D: (a) Expanded metal mesh; (b) Gavazzi mesh.

Table 2. Expanded metal mesh – technical details and material properties.

Product name	Expanded metal mesh plaster wire mesh
Sheet size	1 m × 7 m
Weight	730 gm/m^2
Diamond size	16 mm × 31 mm
Dimensions of strand	1.25mm × 1.5mm
Proof Stress (N/mm^2)	199
Proof Strain (×10^{-3})	9.7
Ultimate Strength (N/mm^2)	320
Ultimate Strain (×10^{-3})	59.2

Table 3. Gavazzi mesh – technical details and material properties.

Product name	Gavazzi 0133-A	
Mesh openings	Approx. 12.5 mm × 11.5 mm	
Weight	120 gm/m^2 ± 5%	
Composition	Fiberglass approx. 82 %	
	Alkali-resistant finish approx. 18 %	
Resistance to tensile strength	Breaking strength	Elongation
	Warp approx. 1650 N/5 cm	5 % ± 1
	Weft approx. 2000 N/5 cm	5 % ± 1

The dimensions of the tested beams were identical to those of the previous study referenced in. The beams' fixed dimensions were as follows: length of 2200 mm, breadth of 200 mm, flange thickness of 40 mm, height of 170 mm, and web thickness of 30 mm, resulting in a total height of 250 mm for each specimen. The beams were loaded under a four-point load setup until failure, with 2000 mm between the two supports and 660 mm between the two loads. The choice of a four-point loading test is motivated by the suitability of the flexural test for assessing the strength of brittle materials, as it subjects the material to a pure bending load. This type of loading test holds particular significance in the examination of brittle materials, where the quantity and severity of flaws exposed to maximum stress directly influence flexural strength and crack initiation. In comparison to the three-point bending flexural test, the four-point loading test eliminates shear forces in the area between the two loading supports. Additionally, the utilization of a four-point loading test serves the purpose of evaluating how

much the mesh contributes to the manifestation of noticeable deformation before failure. Fig. 2 illustrates the sizes of the tested beams, while Fig. 3 shows the mesh pattern used during the production of the beams and up to the completion of casting.

The two primary factors examined were the type of meshes used and the number of openings in the web of the beam. The beams were intentionally weakened in the shear and moment zones by introducing openings. This was done to investigate the impact of these openings on the behavior of ferrocement I-beams reinforced with various types of metallic and non-metallic meshes. On the opposite side, the opening area was chosen to be small enough not to interfere with the beam's effectiveness while still allowing the necessary wires to pass-through.

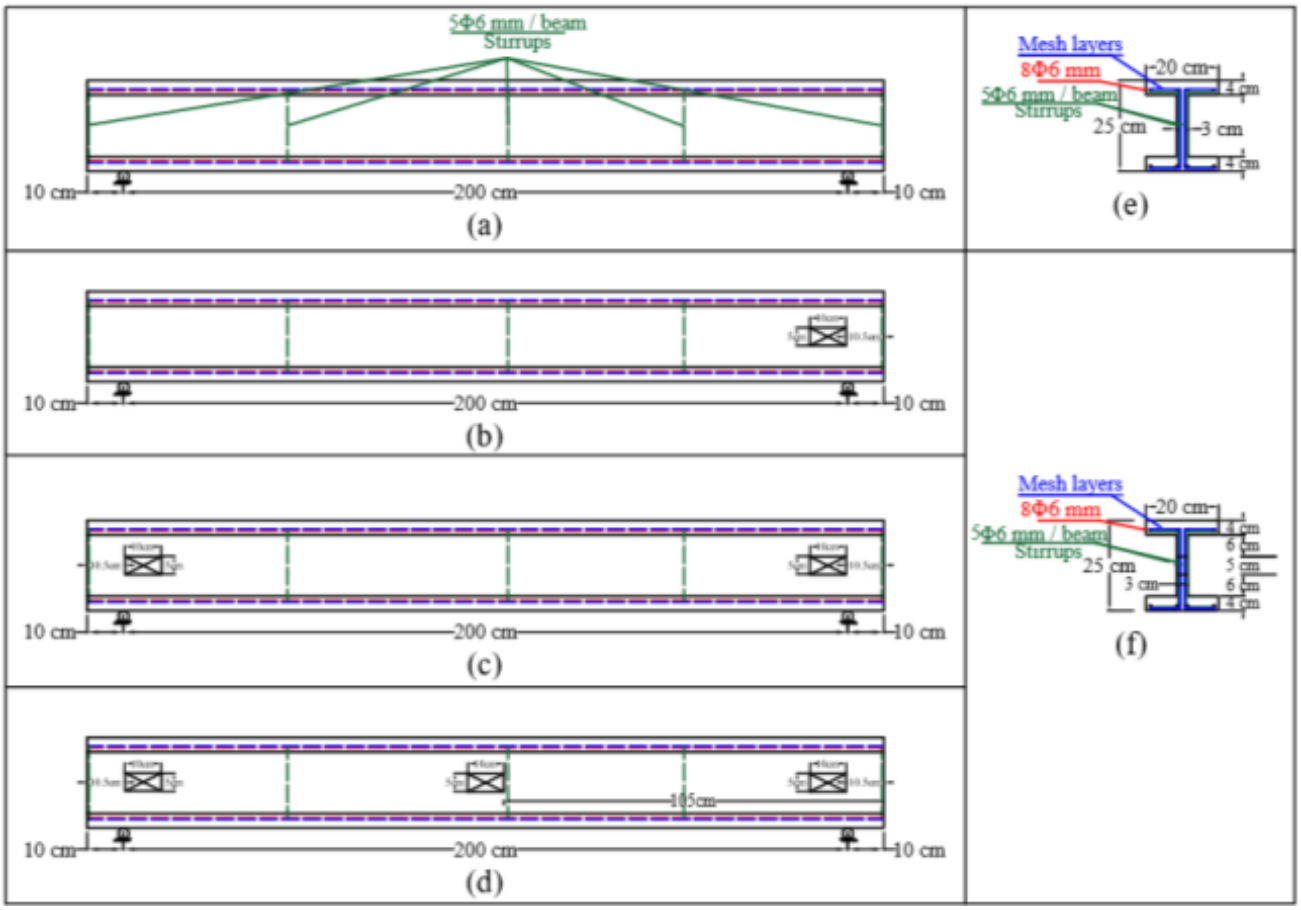

Fig. 2. Geometric **s**pecifications of **e**xamined beams and openings:
(a) Control beam; (b) Beams with one opening; (c) Beams with two openings; (d) Beams with three openings; (e) Side view of control beam; (f) Side view of beams with openings.

Fig. 3. The configuration of meshes employed in the preparation process:
(a) Beams featuring expanded metal mesh reinforcement; (b) Beams reinforced with Gavazzi mesh.

Throughout the testing procedure, the recorded data included the vertical displacement plotted against the applied load. The testing apparatus comprised loading cells, a control station, and a testing frame. Incremental loadings of 5.0 to 20 kN were systematically applied to each specimen. At each stage of loading, meticulous measurements of cracking patterns and deformation values were conducted. The experimental program took place in the laboratory of properties and testing materials at the Faculty of Engineering, Menoufia University, Egypt. The mixing method, curing conditions, and testing techniques employed mirrored those utilized in a previous study by the same authors.

3. Test Set-up and Instrumentation

Following a 28-day period, the beams were coated with white to facilitate the identification of cracks. For strain measurement against load, four demec points were strategically positioned on both the upper and lower flanges of the beam's mid-span on one side, as illustrated in Fig. 4. The measurements were then multiplied by the gauge coefficient of the mechanical gauge in use to estimate the strain values, and the dial gauge values at each load increment were recorded to calculate the beam deflection.

(a)

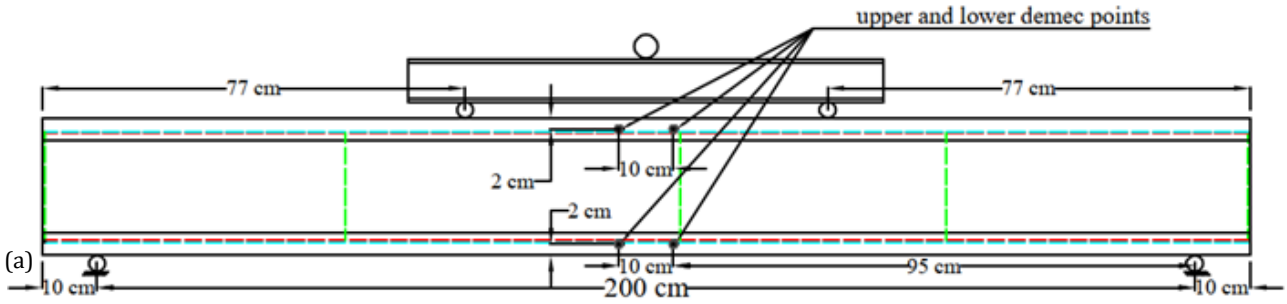

(b)

Fig. 4. Test setup: (a) Locations of the applied loads, and placement of demec points on the tested specimen; (b) Beam G0 under loading.

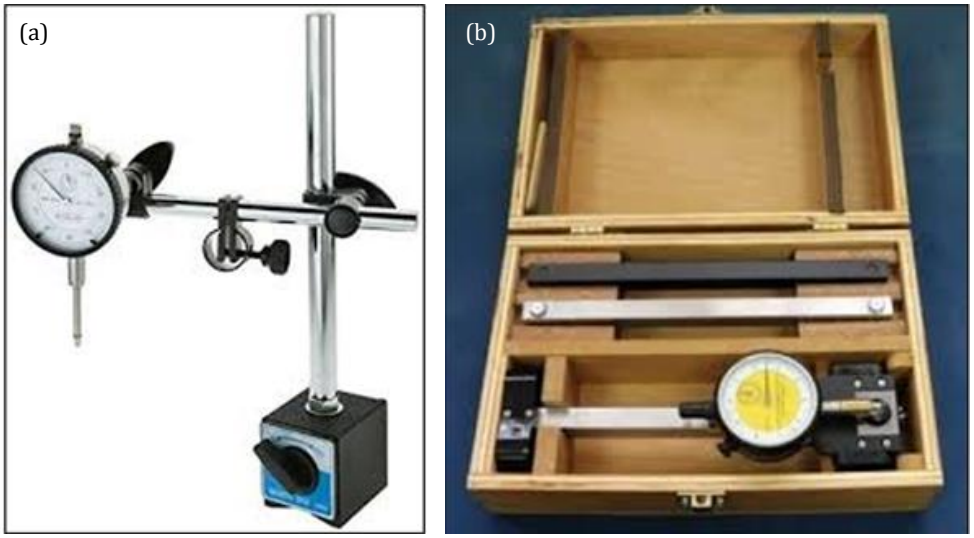

Fig. 5. Dial and deflection gauges used: (a) Dial gauge; (b) Strain gauge.

The specimen was positioned at the center of the testing apparatus, maintaining a uniform distance equals 2000 mm between the specimen supports. As depicted in Fig. 4, the applied loads were situated 770 mm away from each of the beam's ends. Fig. 5 displays the deflection and dial gauges utilized in the test

4. Finite Element Model

To validate the obtained findings and gain a better understanding of the performance of I-shaped ferrocement beams incorporating web perforations, finite element models were developed using Abaqus 6.14, in addition to experimental investigations. For this purpose, a 3D finite element model was created using Abaqus to study the nonlinear material and geometric responses of concrete, steel bars, and reinforced meshes.

4.1. Mesh size and element description

The brick element (C3D8R) shown in Fig. 6 was used to model the ferrocement I-beams. In contrast, the T3D2 element shown in Fig. 7, which is a three-dimensional line element with two nodes, was employed to simulate the steel bars, welded metal mesh, expanded metal mesh, and Gavazzi mesh. These elements are typically used in continuum elements, particularly in concrete members according to Abaqus user's guide (2014). In a recent article, Hekal et al. (2023) have recommended the use of C3D8R and T3D2 elements for beam modeling. On the other hand, to ensure precise simulation of the Tensar mesh, the shell element S4R depicted in Fig. 8 was utilized. The S4R element was chosen specifically to accurately represent the shape of the Tensar mesh.

Additionally, the models were partitioned into elements of diverse sizes, striking a balance between swift computation and precise analysis. The mesh dimensions used for each model were 10, 15, and 20 mm. Fine elements were strategically concentrated in the central loading region of the beam, as illustrated in Fig. 9. Simultaneously, coarse elements were employed near the edges of the beam. The reason for refining the element size in the middle is attributed to the significance of this area as the load impact zone and the location where deformation values were measured during the practical experiment.

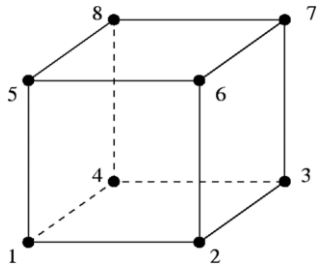

Fig. 6. 8-node 3-D solid (brick) element.

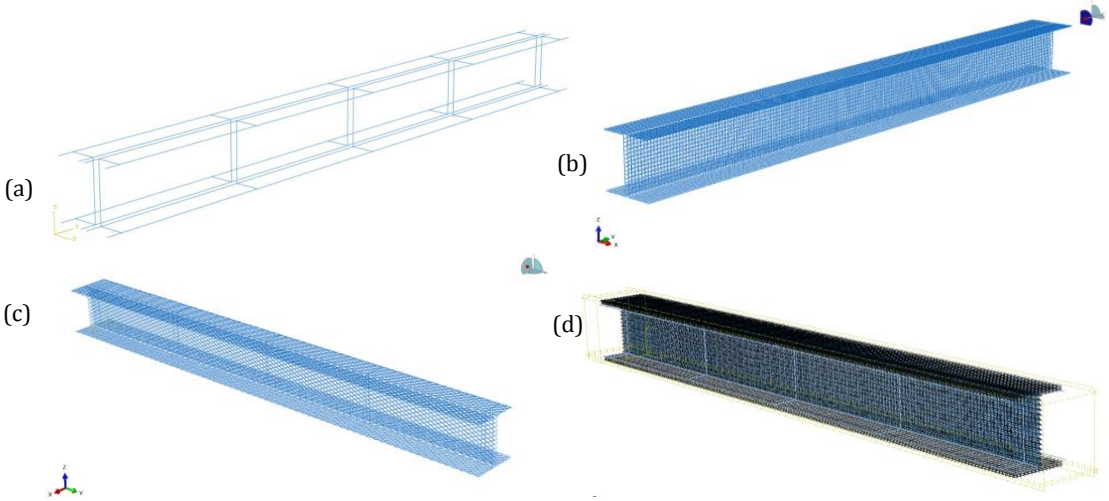

Fig. 7. Modeling of steel bars and reinforcing meshes using truss element: (a) Modeling of steel bars; (b) Modeling of welded metal meshes; (c) Modeling of expanded steel meshes; (d) Modeling of Gavazzi mesh.

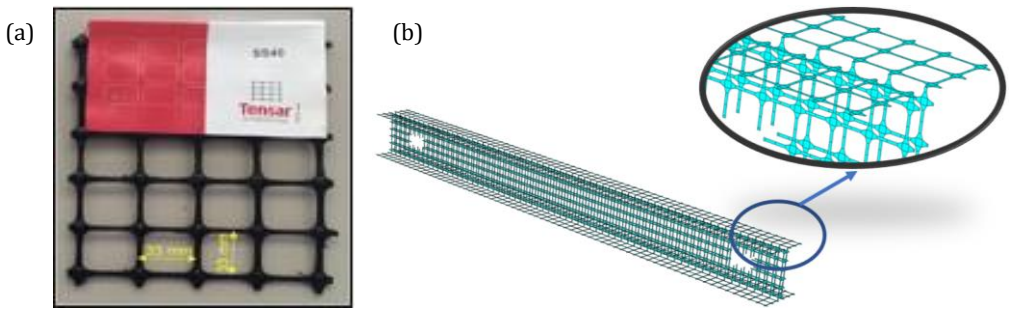

Fig. 8. Modeling of Tensar mesh using shell element:
(a) The real shape of Tensar meshes; (b) The modeling of Tensar using shell element.

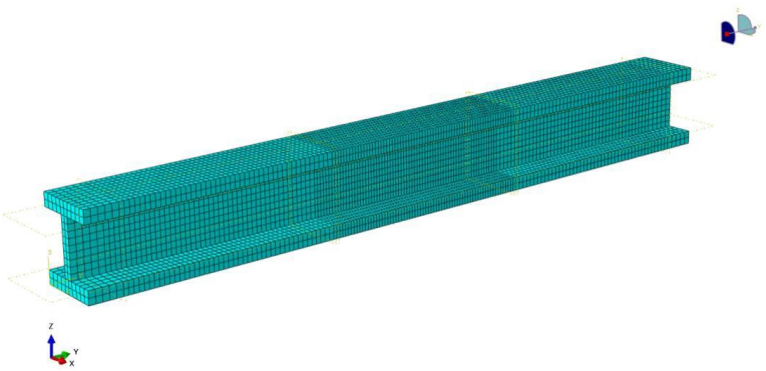

Fig. 9. Mesh representation of the concrete component.

4.2. Modeling of materials

Despite providing material characteristics for all elements, acquiring high-quality material information can be challenging, especially for more intricate material models like those involving material damage properties. The precision and comprehensiveness of pertinent data significantly influence the credibility and validity of the results.

To model the ferrocement I-beams, three different material models from Abaqus were used according to Abaqus User's Guide (2014). These include the concrete-damaged plasticity and the elastic-plastic models.

4.2.1. Concrete damaged plasticity model (CDP)

The Abaqus CDP model was chosen for the concrete material representation. This model incorporates the principles of isotropic damage elasticity, combined with isotropic compression and tensile plasticity, to simulate the inelastic behavior of concrete.

As illustrated in Fig. 10, the CDP model is used to indicate the uniaxial tension and compression behavior of concrete. When failure stresses are reached in the concrete, they are transformed into micro cracks in the concrete blocks. After the point of failure stress in concrete, the stress-strain behavior is influenced by the softening characteristic, depicted in Fig. 10(a). The response to uniaxial compression is linear until the initiation of yield (F_{cu}). Concrete exhibits stress hardening, succeeded by strain softening after attaining the ultimate stress (F_{cu}) within the plastic zone, as illustrated in Fig. 10(b). Consequently, concrete stresses dictate the unloading process from any given point on the strain curve.

$$f_t = E_c\,(\varepsilon_t - \varepsilon_t^{pl})\,(1 - dt) \tag{1}$$

$$f_c = E_c\,(\varepsilon_c - \varepsilon_c^{pl})\,(1 - dc) \tag{2}$$

where E_c is the modulus of elasticity of concrete. Then, the effective tensile and compressive cohesion stresses of concrete are estimated as:

$$\dot{f}_c = \frac{f_c}{(1-dc)} = E_c\left(\varepsilon_c - \varepsilon_c^{pl}\right) \tag{3}$$

$$\dot{f}_t = \frac{f_t}{(1-dt)} = E_c\left(\varepsilon_t - \varepsilon_t^{pl}\right) \tag{4}$$

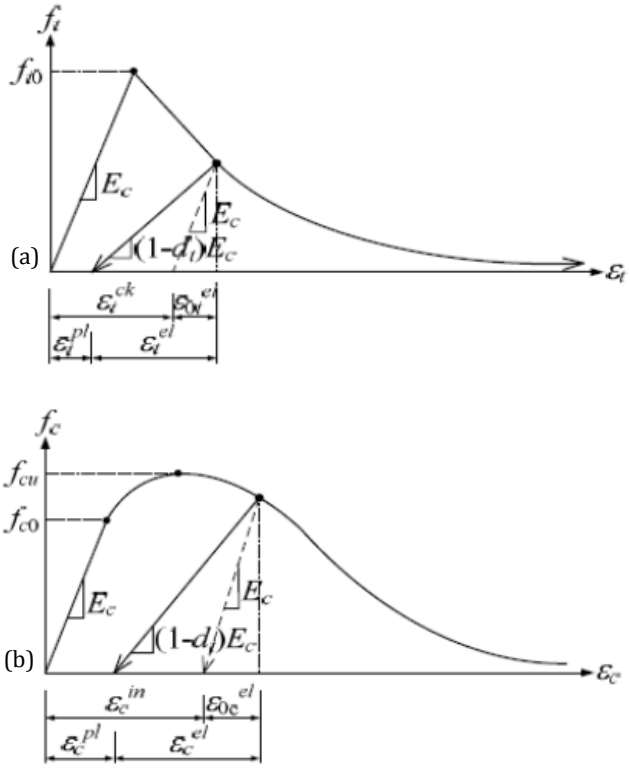

Fig. 10. Concrete damage plasticity behavior: (a) Tensile behavior associated with tension stiffening; (b) Compressive behavior associated with compression hardening.

The behavior of reinforced concrete after failure is illustrated by the post-failure stress, which is influenced by cracking strains ε_t^{ck} and ε_c^{ck}. These strains are characterized as the total strain minus the elastic strain associated with undamaged material, and tension stiffening information is presented concerning the cracking strains. In instances where unloading data is present, the programming automatically transforms cracking strain values into plastic strain values using predefined relationships:

$$\varepsilon_t^{pl} = \varepsilon_t^{ck} - \frac{d_t}{(1-d_t)} \times \frac{f_t}{E_c} \tag{5}$$

$$\varepsilon_c^{pl} = \varepsilon_c^{ck} - \frac{d_c}{(1-d_c)} \times \frac{f_c}{E_c} \tag{6}$$

Tables 4 and 5 list concrete elastic properties and CDP model parameters used in the analysis. The modulus of elasticity of concrete was determined according to the next formula:

$$E_c = 4400\sqrt{F_{cu}} \quad (\mathrm{N/mm^2}) \tag{7}$$

where, F_{cu} is the average compressive strength of the standard cubes at 28 days.

Table 4. Elastic characteristics of the concrete.

Parameter	Value
Density	2.2×10^{-9} N/mm^3
Modulus of elasticity (E_s)	26×10^3 MPa
Poisson's ratio (υ)	0.2

Table 5. Concrete damaged plasticity parameters.

Parameter	Value
Dilation angle	40°
Eccentricity	0.11
f_{b0}/f_{c0}	1.36
K	0.68
Viscosity parameter	0.00001

4.2.2. Elastic-plastic model

Steel bars as well as metal meshes were simulated using a linear elastic-plastic model, as depicted in Fig. 11. The linear behavior signifies the elastic phase up to the yield point, succeeded by the hardening phase representing the plastic stage up to the ultimate load. The mechanical properties of the steel bars, in accordance with E.S.S. 262 (2011), and the specification of the metal meshes used for modeling, as provided by the manufacturer, are detailed in Table 6.

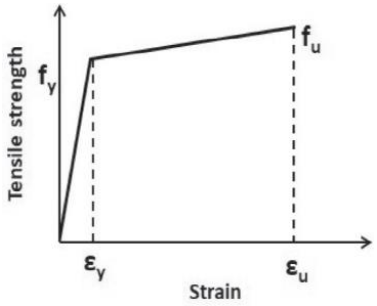

Fig. 11. The stress-strain curve for the steel.

As non-metal meshes exhibit brittle characteristics, and their stress-strain curves lack plastic deformation prior to abrupt failure, they were represented as elastic materials in the model. In Abaqus, the proof stress for each material was defined to determine the failure point during analysis. Table 7 presents the mechanical properties of the non-metal meshes utilized for modeling according to the manufacturer.

Table 6. Mechanical characteristics of steel bars and metal meshes.

Steel 24/35		Welded mesh		Expanded mesh	
Mass density, kg/m^3		Mass density, kg/m^3		Mass density, kg/m^3	
7859		7800		7800	
E, MPa	Poisson's ratio, υ	E, MPa	Poisson's ratio, υ	E, MPa	Poisson's ratio, υ
205×10^3	0.3	170×10^3	0.28	130×10^3	0.28
Stress, MPa	Plastic strain	Stress, MPa	Strain	Stress, MPa	Strain
240	0	413	0	199	0
350	0.0951	610	0.05763	320	0.0495

Table 7. Mechanical properties of non-metal meshes.

Tensar mesh		Gavazzi mesh	
Mass density, kg/m^3		Mass density, kg/m^3	
1590		1210	
E, MPa	100×10^3	E, MPa	80×10^3
Poisson ratio	0.3	Poisson ratio	0.3
Proof stress, MPa	198.43	Proof stress, MPa	325

4.3. Boundary conditions and load application

The supports of the ferrocement I-beam were restrained from translating in the YZ directions and rotating about the XZ plan at the two contact lines beneath the roller supports. Two line loads were applied to the ferrocement I-beam at a similar distance from the support line. The boundary conditions and loads are depicted in Fig. 12.

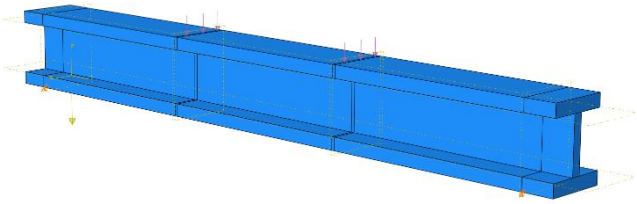

Fig. 12. Simply supported boundary conditions and load applied in the F.E. model.

4.4. Contact definition

The embedded element technique is employed to define an element or a cluster of elements embedded within a set of host elements. According to the Abaqus User's Guide (2014), this method utilizes the response of the host elements to constrain the translational degrees of freedom of the embedded nodes. It is particularly well-suited for modeling truss or beam elements embedded within a set of solid elements. This interaction type was chosen to model the interaction between the concrete beam and reinforced mesh. Fig. 13 depicts the resulting pattern of the beam after applying this interaction technique.

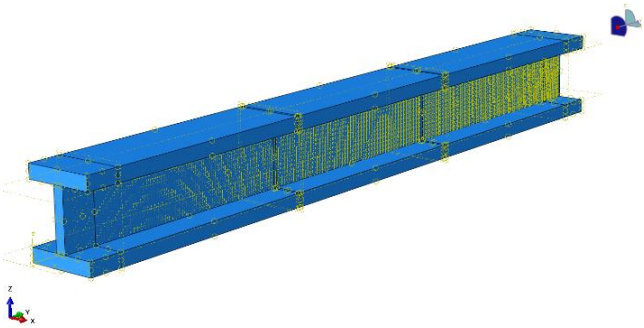

Fig. 13. The beam's pattern after the applying interaction.

5. Comparison of Experimental and Numerical Results

To validate the finite element model developed for this study, a comparison is made between the numerical and experimental results.

5.1. Initial crack loads, ultimate loads, and peak deflections of tested beams

Table 8 presents the findings of experimental and FE model for the initial crack loads, ultimate loads, and mid-span deflections of the tested beams. The results demonstrate that FE simulations yield accurate and compatible results when compared to experimental results. The average first crack load difference as a percentage is approximately 5.5%, while the average ultimate load difference is approximately 5%. Furthermore, the average difference in maximum deflections between the experimental and FE results is approximately 5.8%. Fig. 14 illustrates the relationships between the applied load and both experimental and FE first crack loads, ultimate loads, and maximum deflections of all tested beams.

As depicted in Fig. 14, Beam G0 demonstrated the highest ultimate load at 48.33 kN, while Beam T3 exhibited the lowest ultimate load at 34.45 kN. Additionally, Beam G0 recorded the maximum first cracking load of 14.50 kN, whereas Beam W3 had the minimum first cracking load of 9.59 kN.

Comparing beams with Gavazzi meshes to those with welded steel meshes, Gavazzi meshes exhibited a higher ultimate load by 3.8%, 8.6%, and 3.9% for beams without openings, one opening, and two openings, respectively. Furthermore, beams with Gavazzi meshes displayed a higher ultimate load compared to beams with expanded metal meshes by 9.2%, 10.1%, and 2.5% for beams without openings, one opening, and two openings, respectively.

In the comparison of non-metal meshes, Gavazzi meshes demonstrated a higher ultimate load than Tensar meshes by 23.2%, 21.3%, 15.6%, and 10.2% for beams without openings, one opening, two openings, and three openings, respectively. This outcome is likely attributed to the superior properties of Gavazzi meshes as non-metallic materials, enhancing the performance of the beams more effectively than other mesh types. Regarding the comparison between metal meshes used, beam W0 exhibited a higher deflection than beam E0 by 3.3%, while beams W1, W2, and W3 exhibited lower deflections than beams E1, E2, and E3 by 3.2%, 5.7%, and 11.3%, respectively. In addition, when comparing non-metal meshes used, beams G0, G1, G2, and G3 exhibited higher deflections than beams T0, T1, T2, and T3 by 5.2%, 3.3%, 9.5%, and 5.9%, respectively.

From Fig. 14, it was observed that the first crack load of beams T2 and T3 was higher than the first crack load of beams T0 and T1.

5.2. Ductility ratio

The ductility ratio, representing the relationship between the mid-span deflection at the ultimate load and that at the first crack load, was computed for each tested beam. The results are tabulated in Table 9, and a visual representation is depicted in Fig. 15. As shown in Fig. 15, for beams without openings and with one opening, those reinforced with welded metal mesh have a higher ductility ratio compared to their counterparts in other groups, while for beams with two and three openings, beams reinforced with expanded meshes have higher ductility ratios compared to the other beams with two and three openings. This may be due to the higher maximum deflection values of welded beams without openings and with one opening and beams reinforced with expanded

meshes with two and three openings, while the deflection at first crack loads of welded beams without openings and with one opening and beams reinforced with expanded meshes with two and three openings is close to the deflection at first crack loads of the other beams. In addition, as shown in Fig. 15, beam W0 had the highest ductility ratio among all the tested beams, while beam G3 obtained the lowest ductility ratio. This finding is supported by a previous study conducted by Shaaban et al. (2018) that showed that beams reinforced with Gavazzi meshes had the lowest ductility ratio when compared to beams reinforced with steel meshes. The results indicate that the FE simulations achieve accurate and consistent results when compared to the experimental results, with a mean difference of 2.2% between the investigational and FE ductility ratios.

Table 8. Comparative analysis of first crack loads, ultimate loads, and maximum deflection between experimental and finite element results.

Group name	Code of the beams	First crack load (kN)			Ultimate load (kN)			Maximum deflection (mm)		
		Experimental	F.E.	Difference (%)	Experimental	F.E.	Difference (%)	Experimental	F.E.	Difference (%)
A	W0	11.15	11.73	5.2	45.11	46.56	3.2	12.50	12.80	2.4
	W1	10.23	10.72	4.8	41.25	42.56	3.2	10.90	11.24	3.6
	W2	9.65	10.16	5.3	37.98	40.31	6.1	9.74	10.46	7.4
	W3	9.04	9.59	6.0	35.42	38.04	7.4	9..00	9.55	6.2
B	T0	10.96	11.54	5.3	36.97	39.24	6.1	6.75	7.28	7.8
	T1	10.74	11.20	4.3	36.19	38.11	5.3	6.64	7.20	8.5
	T2	13.13	13.94	6.2	34.52	36.22	4.9	5.81	6.24	7.4
	T3	12.58	13.26	5.4	33.6	34.45	2.5	5.68	5.92	4.3
C	E0	10.79	11.16	3.4	42.64	44.26	3.8	11.94	12.39	3.8
	E1	10.00	10.58	5.8	39.75	41.98	5.6	10.81	11.61	7.4
	E2	9.86	10.29	4.4	38.76	40.84	5.4	10.75	11.09	3.2
	E3	9.22	9.97	8.1	36.78	39.56	7.6	9.99	10.77	7.8
D	G0	14.02	14.50	3.4	46.88	48.33	3.1	7.28	7.66	5.3
	G1	13.08	13.87	6.0	44.98	46.24	2.8	7.01	7.44	6.1
	G2	11.76	12.56	6.8	39.68	41.88	5.5	6.34	6.83	7.6
	G3	10.63	11.39	7.2	35.39	37.97	7.3	6.00	6.27	4.5

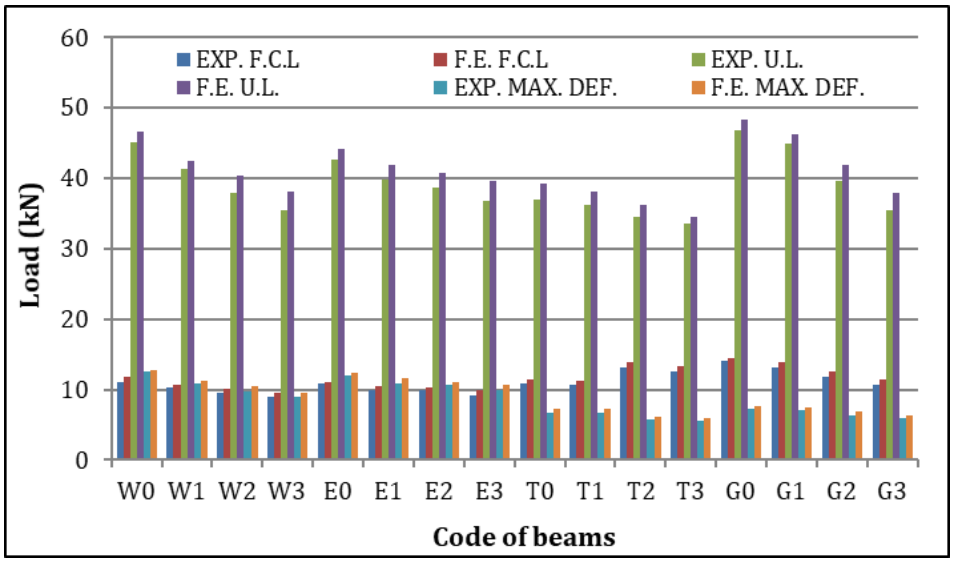

Fig. 14. The relation between the applied load and both experimental F.C.L., F.E. F.C.L., experimental U.L., F.E. U.L., experimental maximum deflection, and F.E. maximum deflection of all tested beams.

Table 9. Comparison between the experimental and F.E. results of ductility ratio, and load-to-weight ratio.

Group name	Code of the beams	Ductility ratio			Load-to-weight ratio (kg/kg)			Energy absorption (kN·mm)		
		Experimental	F.E.	Difference (%)	Experimental	F.E.	Difference (%)	Experimental	F.E.	Difference (%)
A	W0	10.86	11.26	3.6	55.05	56.82	3.2	303.2	320.5	5.7
	W1	9.96	10.26	2.9	50.51	52.10	3.1	238.9	255.2	6.8
	W2	9.49	9.36	1.4	46.65	49.51	6.1	197.4	224.9	13.9
	W3	8.83	8.64	2.2	43.64	46.88	7.4	169.0	192.7	14.1
B	T0	5.56	5.51	0.9	45.12	47.88	6.1	129.1	147.7	7.7
	T1	5.54	5.48	1.1	44.31	46.66	5.3	126.0	143.9	13.5
	T2	7.36	7.48	1.7	42.40	44.49	4.9	122.0	137.4	8.7
	T3	7.19	7.48	3.8	41.40	42.46	2.6	117.7	125.9	16.0
C	E0	10.71	10.64	0.6	52.04	54.01	3.8	272.4	293.5	14.4
	E1	10.33	9.91	4.3	48.67	51.40	5.6	229.7	260.7	14.2
	E2	10.02	9.86	1.6	47.61	50.16	5.4	221.7	241.1	12.6
	E3	9.82	9.51	3.3	45.32	48.75	7.6	196.0	227.4	6.9
D	G0	6.00	5.91	1.4	57.21	58.99	3.1	176.3	191.5	8.6
	G1	5.94	5.85	1.7	55.07	56.61	2.8	164.1	179.0	9.0
	G2	5.72	5.47	4.7	48.74	51.44	5.5	132.2	150.2	13.6
	G3	5.44	5.40	0.7	43.61	46.79	7.3	112.3	125.9	12.1

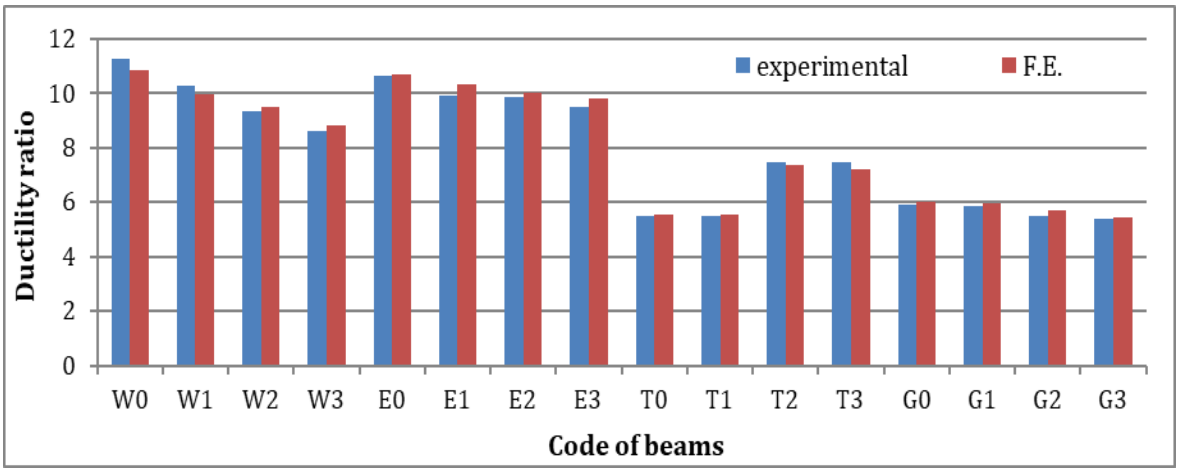

Fig. 15. Experimental and F.E. ductility ratio of all tested beams.

5.3. Load versus deflection relationships

Table 8 presents the ultimate load and maximum central deflection for each tested beam, while Figs. 16 to 20 depict the relationship between applied load and central deflection for each examined beam.

Analyzing the figures reveals that, for beams without openings, beam W0 exhibited a higher deflection than others, with a 3.3%, 75.9%, and 67.0% increase compared to beams E0, T0, and G0, respectively. Similarly, in beams with one opening, beam E1 had a higher deflection, with a 3.3%, 61.2%, and 56.1% increase compared to beams W1, T1, and G1, respectively. Additionally, in beams with two openings, beam E2 showed a higher deflection, with a 6.1%, 77.8%, and 62.5% increase compared to beams W2, T2, and G2, respectively. Finally, for beams with three openings, beam E3 had a higher deflection, with a 12.7%, 82.0%, and 71.9% increase compared to beams W3, T3, and G3, respectively.

Figure 17 highlights that within the 5 kN to 30 kN load range, the deflection of beams T2 and T3 is consistently lower than that of T0 and T1. This difference may be attributed to the fact that in T0 and T1, failure occurred primarily due to bending, leading to higher bending moment values and subsequently elevated deflection values. Conversely, in T2 and T3, stresses were distributed

around the openings in the shear zone, resulting in lower deflection values.

Comparing maximum deflection values, for welded steel meshes, beams W3, W2, and W1 had lower values than W0, with a decrease of 25.3%, 18.3%, and 12.2%, respectively. Similarly, for expanded metal meshes, beams E3, E2, and E1 had lower values than E0, with a decrease of 13.1%, 10.5%, and 6.3%, respectively. In the Tensar meshes group, beams T3, T2, and T1 had lower values than T0, with a decrease of 18.7%, 14.3%, and 1%, respectively. Finally, for the Gavazzi meshes group, beams G3, G2, and G1 had lower values than G0, with a decrease of 18.2%, 10.9%, and 2.9%, respectively.

In conclusion, the detailed analysis suggests that the configuration of openings, the specific arrangement of mesh types, and the distribution of stress in shear and bending zones play pivotal roles in determining the deflection behavior of the tested beams. This information is crucial for optimizing beam design and understanding the interplay between structural elements in real-world applications.

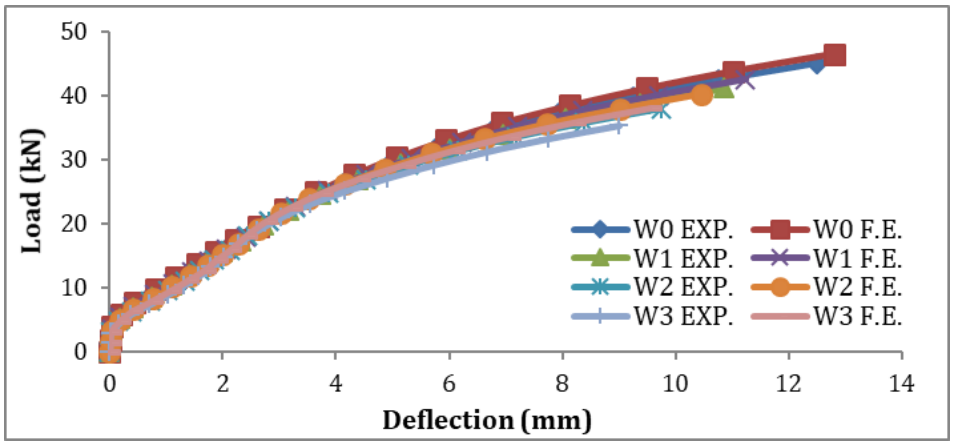

Fig. 16. Load-deflection curves of the group (A).

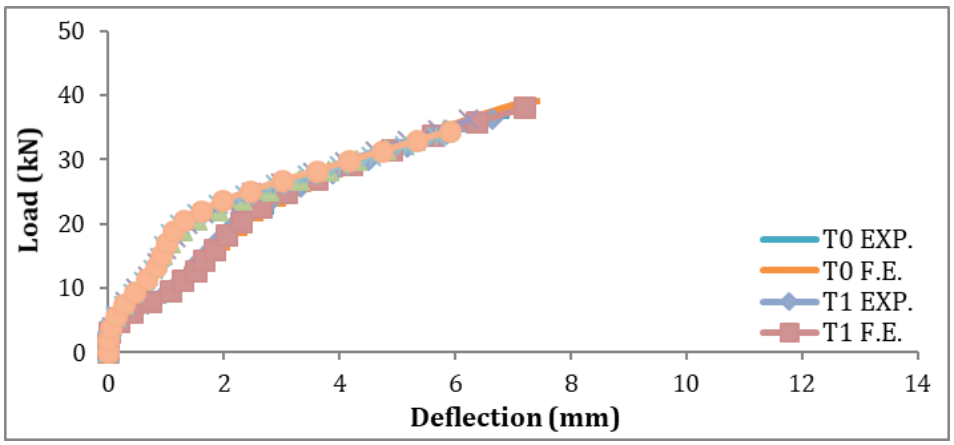

Fig. 17. Load-deflection curves of the group (B).

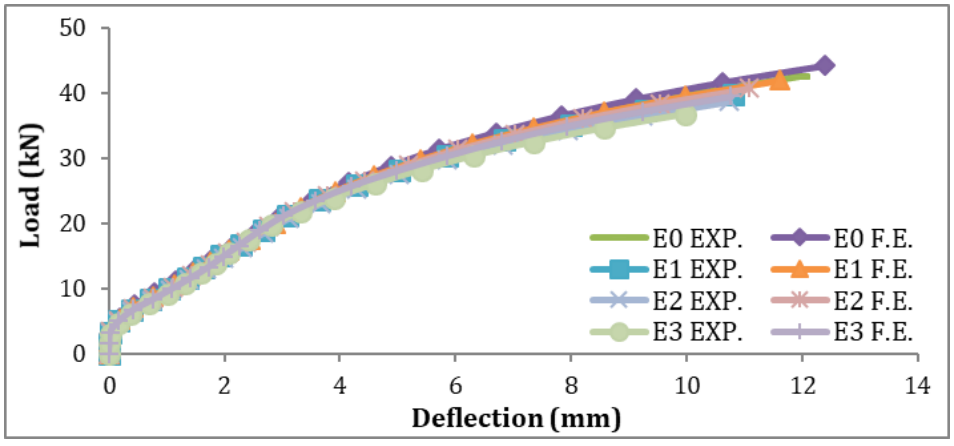

Fig. 18. Load-deflection curves of the group (C).

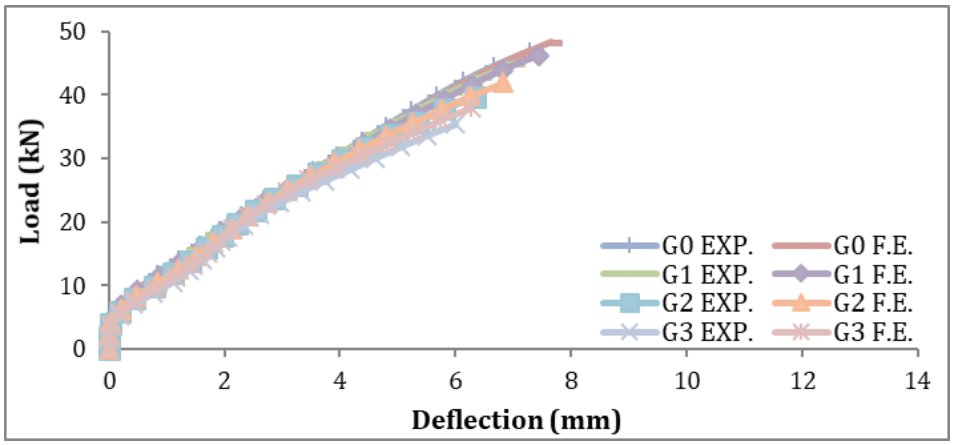

Fig. 19. Load-deflection curves of the group (D).

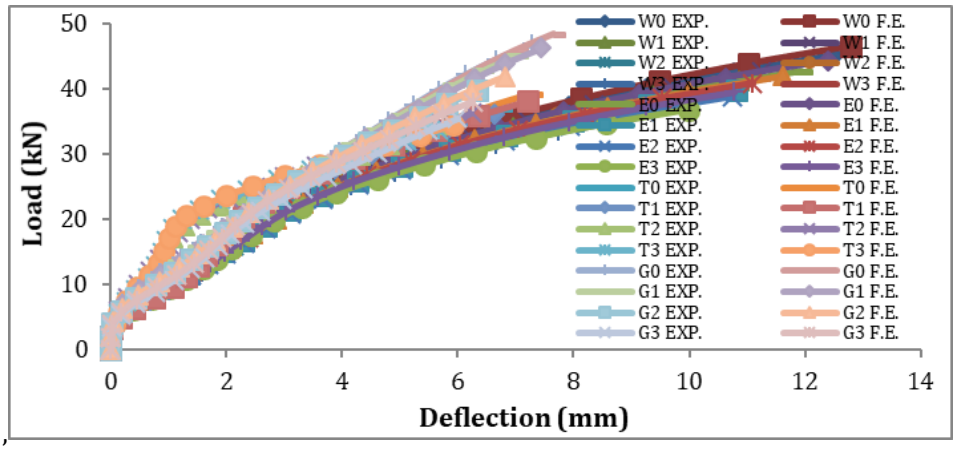

Fig. 20. Load-deflection curves of all tested beams.

5.4. Energy absorption

The quantity of energy absorbed by a beam is depicted by the area beneath its load-deflection curve. To compute this area, the load-deflection curve equation for each beam specimen was integrated using a computer program written in the BASIC language, outlined as follows:

$$\text{Ultimate load energy absorbed} = \int_0^{\Delta u} f(\Delta)\, d\Delta \qquad (8)$$

where $f(\Delta)$ represents the load defection curve equation.

The integration was performed from zero deflection to the mid-point deflection at the failure load, represented by the symbol u. The energy absorbed by each beam is listed in Table 9 and shown graphically in Fig. 21. From the figure, it can be observed that beam W0 absorbed the most energy among all the tested beams, while beam G3 absorbed the least. This is due to the large area beneath the load-deflection curve of beam W0 and the small area under the load-deflection curve of beam G3.

5.5. Load-to-weight ratio

To investigate the effect of the opening number on the performance of beams, the load-to-weight ratio was determined by dividing the ultimate load by the weight of the beams. The load-to-weight ratio values for all tested beams are presented in Table 9 and shown in Fig. 22. The results indicate that as the number of openings increases, the load-to-weight ratio decreases. Specifically, for welded, expanded metal, Tensar, and Gavazzi beams, placing three openings decreased the load-to-weight ratio by 17.5%, 9.7%, 11.3%, and 20.7%, respectively, compared to beams without openings. Placing two openings decreased the load-to-weight ratio by 12.9%, 7.1%, 7.1%, and 12.8%, respectively. Additionally, placing one opening in beams with dimensions of 100×50 mm reduced the load-to-weight ratio by 8.3%, 4.8%, 2.5%, and 4.0% for welded, expanded metal, Tensar, and Gavazzi beams, respectively, compared to beams with no openings. The reduction in load-to-weight ratios is proportional to the volume of openings in the beams.

5.6. Effect of openings on the performance of tested beams

When comparing various types of metal mesh, it was observed that the ultimate load in beams with three openings decreased by 18.3% for welded steel mesh beams and by 10.6% for expanded metal mesh beams, compared to beams without openings. In contrast, concerning non-metal meshes, the ultimate load in beams with three openings decreased by 21.4% for Gavazzi

mesh beams and by 12.2% for Tensar mesh beams compared to beams without openings.

Introducing three openings in beams with dimensions of 100×50 mm resulted in a reduction of maximum deflection by 28%, 16.3%, 15.9%, and 17.6% for welded beams, expanded beams, Tensar beams, and Gavazzi beams, respectively, compared to beams without openings. Furthermore, placing three openings in these beams reduced the ductility ratio by 23.3%, 10.6%, and 8.6% for welded beams, expanded beams, and Gavazzi beams, respectively. Energy absorption was also reduced by 39.9%, 22.5%, 14.8%, and 34.3% for welded beams, expanded beams, Tensar beams, and Gavazzi beams, respectively, when three openings were introduced in beams with dimensions of 100×50 mm, compared to beams without openings.

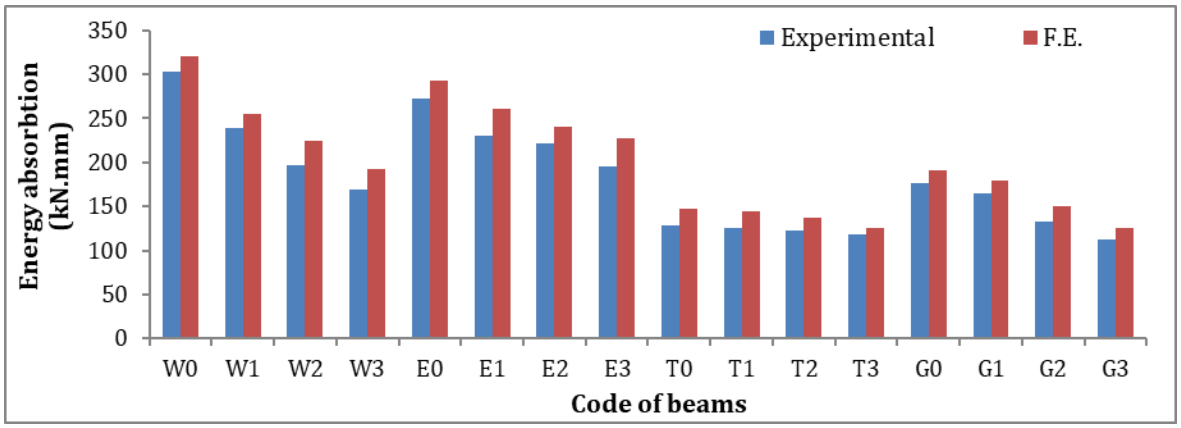

Fig. 21. The energy absorbed by all examined beams.

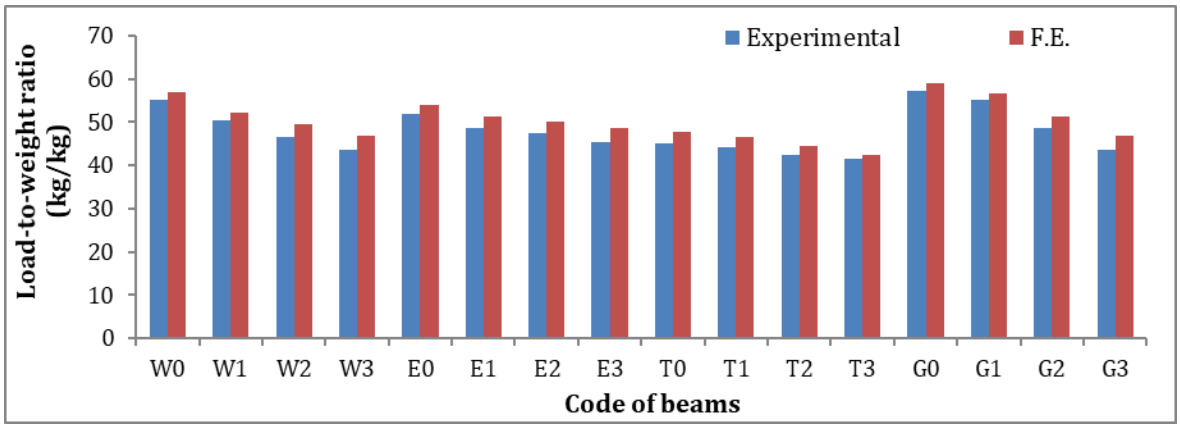

Fig. 22. Experimental and F.E. load-to-weight ratio of all tested beams.

5.7. Cracking patterns and mode of failure

The surface of the beams was inspected, and cracks were identified and marked. The initial crack load, crack propagation, and failure mode were determined for each beam. Flexural cracks appeared near the center of the beam and widened vertically as the load increased. New flexural cracks appeared rapidly and spread wider as the beam approached its failure load. Although most cracks did not reach the top surface of the beam, the crack at midspan grew vertically towards it. Fig. 23 illustrates the cracking shapes and mode of failure for all tested beams. The cracking patterns and mode of failure for beams with openings reinforced by welded steel meshes and expanded metal meshes appear to be a combination of shear and bending failure, with the greatest effect due to bending. In contrast, the cracking patterns and mode of failure for beams with openings reinforced by Tensar meshes and Gavazzi meshes appear to be mainly due to bending.

6. Conclusions

This paper investigates the impact of web openings on the structural behavior of ferrocement I-beams reinforced with metallic or non-metallic meshes. Sixteen beams were cast and tested to study their behavior under flexural loading. The tested beams were grouped into four groups based on the type of reinforcing mesh used, with each group consisting of four beams with the same reinforcement bars and meshes, but with different numbers of web openings.

Welded metal meshes and expanded steel meshes were used as reinforcing meshes for groups A and C, respectively, while Tensar meshes and Gavazzi meshes were used for groups B and D, respectively. To maintain a constant reinforcement weight, the four groups were reinforced with three layers of welded steel meshes, two layers of expanded metal meshes, two layers of Tensar meshes, and eight layers of Gavazzi meshes.

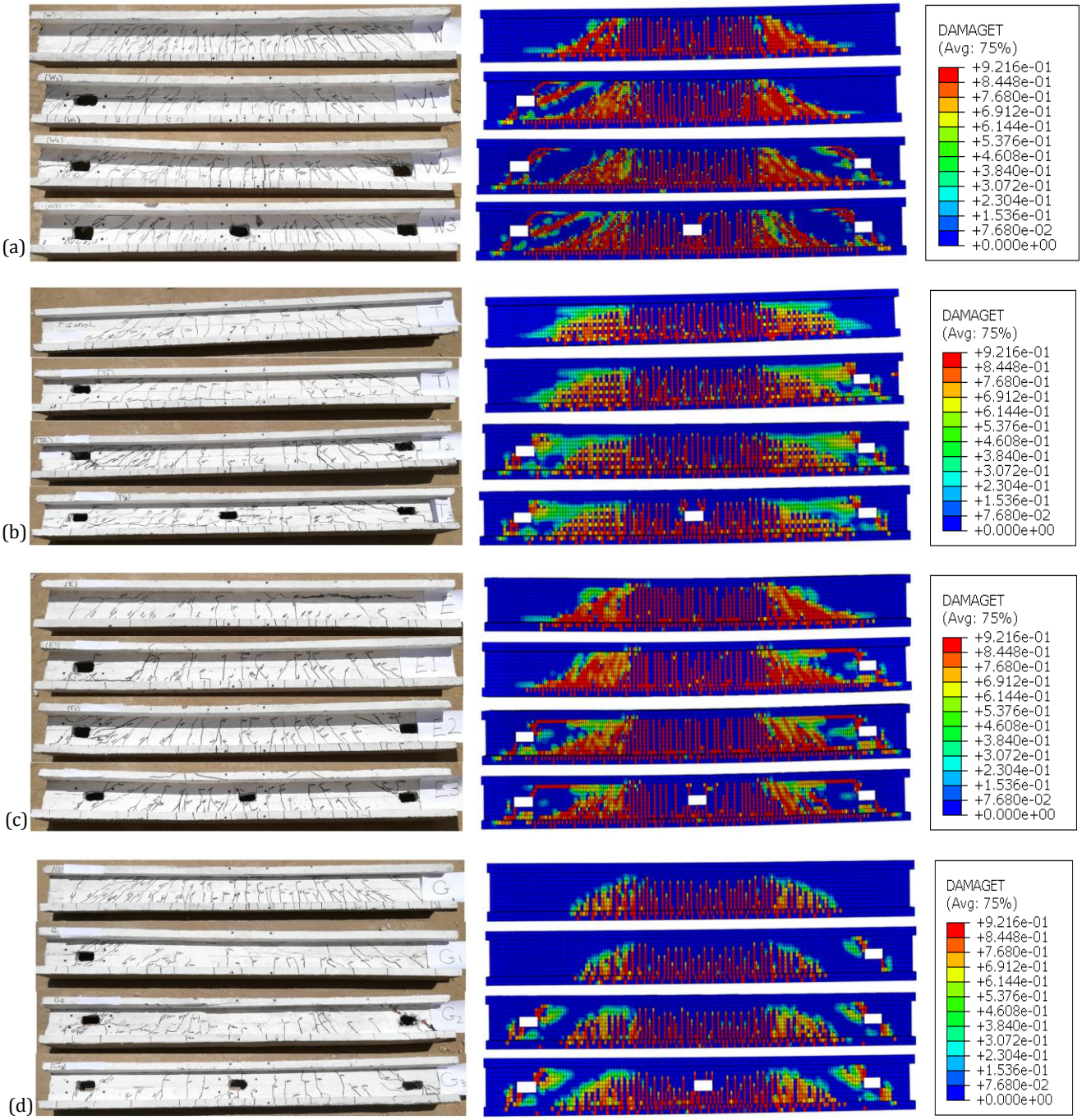

Fig. 23. Experimental and F.E. crack pattern of the tested beams: (a) Group A; (b) Group B; (c) Group C; (d) Group D.

A three-dimensional finite element model was developed, taking into account the nonlinear material behavior of the reinforcing metal mesh and concrete. The model was validated using the experimental test results and showed good agreement.

The results showed that beams with no openings, one, and two openings reinforced with Gavazzi meshes had the highest ultimate load compared to other tested beams, while beams with three openings, those reinforced with expanded metal meshes had the greatest ultimate loads. Placing three openings in beams, with dimensions of 100×50 mm (two of these openings are approximately 10 cm apart from each edge while the third opening is located at mid-span), reduced the load-to-weight ratio by about 20.7%, 12.9%, 8.2%, and 23.8% for welded beams, expanded beams, Tensar beams, and Gavazzi beams, respectively, compared to the beams with no openings.

Based on the experimental and FE results available, the following conclusions can be drawn:

- The efficiency of beams is negatively affected by the presence of openings, resulting in a decrease of ultimate loads by approximately 5.2%, 10.5%, and 15.6% on average for one, two, or three openings, respectively, compared to beams without openings.
- In the case of beams with one, two, and three openings, the utilization of expanded metal meshes resulted in a higher ductility ratio and energy absorption capacity compared to other tested mesh types. However, for beams with no openings, the use of

welded steel meshes demonstrated greater ductility and energy absorption while also potentially leading to increased deflection values.

- When considering beams with three openings, the use of expanded metal meshes resulted in a higher ultimate load capacity compared to beams with welded steel meshes, beams with Tensar meshes, and beams with Gavazzi meshes by 4%, 14.8%, and 4.2%, respectively. Moreover, the placement of three openings in such beams decreased the load-to-weight ratio by 20.7%, 12.9%, 8.2%, and 23.8% in welded beams, expanded beams, Tensar beams, and Gavazzi beams, respectively, compared to beams with no openings.
- The deflection values for beams with one, two, and three openings varied depending on the type of reinforcement used. In particular, for beams with one opening, beam E1 had a higher deflection value compared to beams W1, T1, and G1, with deflection increases of 3.3%, 61.2%, and 56.1%, respectively. For beams with two openings, beam E2 showed a higher deflection value compared to beams W2, T2, and G2, with deflection increases of 6.1%, 77.8%, and 62.5%, respectively. Similarly, for beams with three openings, beam E3 demonstrated a higher deflection value compared to beams W3, T3, and G3, with deflection increases of 12.7%, 82.0%, and 71.9%, respectively.
- For the welded steel meshes group, beam W3 demonstrated a lower deflection value than beam W0 by 25.3%, while for the expanded metal meshes group, beam E3 showed a lower deflection value than beam E0 by 13.1%. Beams with welded steel meshes had a higher deflection than the other tested beams for beams without openings, while for beams with one, two, and three openings, beams with expanded metal meshes had a higher deflection than the other tested beams.
- For the Gavazzi meshes group, beam G3 exhibited a lower deflection value than beam G0 by 18.2%, while for the Tensar meshes group, beam T3 demonstrated a lower deflection value than beam T0 by 18.7%.
- Beams with Gavazzi meshes demonstrated a higher ultimate load capacity than beams with Tensar meshes by 23.2%, 21.3%, 15.6%, and 10.2% for beams without openings, one, two, and three openings, respectively. However, the ultimate load capacity in beams with three openings decreased by 21.4% compared to the ultimate load capacity in beams with no openings for Gavazzi mesh beams, whereas it decreased by 12.2% for Tensar mesh beams.
- For beams with no opening, one and two openings, Gavazzi mesh beams exhibited a greater ultimate load than the other tested beams, while for beams with three openings, expanded metal mesh beams demonstrated the greatest ultimate loads. Furthermore, Gavazzi mesh beams showed a higher ultimate load than welded steel mesh beams by 3.8%, 8.6%, and 3.9% for beams without opening, one and two openings, respectively, whereas Gavazzi mesh beams displayed a higher ultimate load than expanded metal mesh beams by 9.2%, 10.1%, and 2.5% for beams without opening, one and two openings, respectively.

Acknowledgements

None declared.

Funding

The authors received no financial support for the research, authorship, and/or publication of this manuscript.

Conflict of Interest

The authors declared no potential conflicts of interest with respect to the research, authorship, and/or publication of this manuscript.

Author Contributions

All of the authors made substantial contributions to conception and design, or acquisition of data, or analysis and interpretation of data; were involved in drafting the manuscript or revising it critically for important intellectual content; and gave final approval of the version to be published.

Data Availability

The datasets created and/or analyzed during the current study are not publicly available, but are available from the corresponding author upon reasonable request.

REFERENCES

Abaqus Documentation User's Guide (2014). Dassault Systemes, Simulia Corp, Providence, USA.

ACI 5492R (2004). Report on thin reinforced cementitious products. American Concrete Institute, Farmington Hills, Michigan, USA.

ACI 549R (1997). State of the art report on ferrocement, Manual of concrete practice. American Concrete Institute, Farmington Hills, Michigan, USA.

Acma LMC, Dumpasan GC, Salva MI, Mansaguiton MP, Supremo RP, Daquiado NFP (2015). Flexural strength and ductility behavior of ferrocement i-beam. Mindanao Journal of Science and Technology, 13, 99-108.

Acma LMC, Mariano C (2014). Development and Application of Ferrocement I-beams. *Ph.D. thesis*, Mindanao State University - Iligan Institute of Technology, Iligan City, Philippines.

Ankit B, Sumit G, Lalit K, Hardik S (2017). A review study of application of ferrocement. *International Research Journal of Engineering and Technology*, 4(6), 1592-1597.

Austriaco RL (2006). Research and innovations on ferrocement in the new millenium: global perspective. *Proceedings of 8th International Symposium and Workshop on Ferrocement and Thin Reinforced Cement Composites*, Thailand, IFS, 77-86.

ChandraSekharRao T, GunneswaraRao TD, RamanaRao NV, Rambabu C (2012). An experimental study on ferrocement box-beams under flexural loading. *International Journal of Emerging Technology and Advanced Engineering*, 2(9), 2250-2459.

E.S.S. 262 (2011). Egyptian standard specifications for steel bars. Ministry of Industry, Cairo, Egypt.

Hekal GM, Salama MI, Elsamak G, Almaadawy AH (2023). Shear behavior of RC beams strengthened with ultra-high-performance fiber-reinforced concrete using finite-element analysis. *Asian Journal of Civil Engineering*, 24, 71–91.

International Ferrocement Society (2001). Ferrocement model code. Thailand, IFS.

Naaman AE (2000). Ferrocement and Laminated Cementitious Composites. Techno-Press 3000, Ann Arbor, Michigan, USA.

Pathak A (2020). Effect of silica fume and fly ash as partial replacement of cement on strength of concrete. *International Conference of Advance Research & Innovatio*, India, 167-170.

Rameshkumar M, Malathy R, Chandiran P, Paramasivam S, Chung IM, Kim SH, Prabakaran M (2022). Study on flexural behaviour of ferrocement composites reinforced with polypropylene warp knitted fabric. *Polymers*, 14(19), 4093.

Safiuddin MD, Zain MFM (2005). Effects of silica fume and fly ash on the properties of high-performance concrete. *Proceedings of the Annual Conference on Canadian Society for Civil Engineering*, Toronto, Canada, 2-4.

Salman WD, Mubarak HM, Mahmood MS (2018). Structural behavior and mechanical properties of ferrocement slab panels incorporating fibers. *International Journal of Civil Engineering and Technology (IJCIET)*, 9(11), 2289-2298.

Shaaban IG, Shaheen YBI, Elsayed EL, Kamal OA, Adesina PA (2018). Flexural behaviour and theoretical prediction of lightweight ferrocement composite beams**.** *Case Studies in Construction Materials*, 9, e00204.

Shaheen YBI, Mohamed AM, Mohamed HR (2016). Structural performance of ribbed ferrocement plates reinforced with composite materials. *Structural Engineering and Mechanics*, 60(4), 567-594.

Shaheen YBI, Mousa M, Gamal E (2020), Structural behavior of lightweight ferrocement walls. *13th International Conference on Civil and Architecture Engineering*, Cairo, Egypt, 1-21.

Shaheen YBI, Eid FM, Mesalam O (2021). Structural behavior of ferrocement concrete plates subjected to flexural and dynamic loadings. *Journal of Engineering Research and Reports*, 21(7), 71-84.

Shaheen YBI, Etman ZA, Elrefy AM (2022a). Structural behavior of ferrocement composite hollow-cored panels for roof construction. *Challenge Journal of Concrete Research Letters*, 13(1), 5-27.

Shaheen YBI, Hekal GM, El Shaboury AM (2022b). Structural behavior of ferrocement I-beams with web openings – experimental study. *Engineering Research Journal, Menoufia University*, 45(4), 581-589.

Shaheen YBI, Etman ZA, Kandil DEA (2023a). Performance of light weight ferrocement composite walls. *Challenge Journal of Concrete Research Letters*, 14(3), 69-88.

Shaheen YBI, Hekal GM, Fadel AK (2023b). Structural behavior of multi-cell ferrocement composite beams. *International Conference on Advances in Structural and Geotechnical Engineering*, Hurghada, Egypt, 1-17.

Sumadi S, Ramli M (2008). Development of Lightweight Ferrocement Sandwich Panels for Modular Housing and Industrialized Building System. Project Report, University Teknologi Malaysia (UTM), Research Vote 73311, Johor, Malaysia.

Suresh V (2004). Application of ferrocement for cost-effective building construction. *Journal of Ferrocement*, 34(4), 445-455.

Challenge Journal of Concrete Research Letters

Research Article

Effect of resin amount on the damping properties of polymer concrete

Arif Ulu [a,*]

[a] *Department of Mechanical Engineering, İstanbul Aydın University, 34295 İstanbul, Türkiye*

ABSTRACT

In the construction and infrastructure sector, efforts are being made to find faster and more efficient materials. Polymer concrete (PC) challenges traditional concrete with its fast setting, durability and abrasion resistance. While studies on PC strength are abundant in the literature, studies on the effects of resin amount on damping capacity are fewer than mechanical performance. In this paper, the effect of resin proportion on damping capacity is investigated by modal tests. PC mixtures in the production with different resin proportions (11–19%) were poured into molds of 10x25x500 mm, using aggregates of up to 3.15 mm in size. After 14 days, the natural frequency and damping ratios of the specimens up to 1000 Hz were determined in modal tests. While the damping ratio (DR) decreased in resin contents up to 17%, the results of the specimens with 19% resin ratio increased. However, when the products with the same resin ratio are analyzed, the random distribution of the aggregate affects the damping capacity. The main reason of negative correlation between resin amount and DR is the filler amount in the mixture. Because of the production consistency, fluidization of all the mixtures is prevented by adding fillers. Therefore, the impact of the resin amount on DR is limited or even negative. Besides that, to compare measurement results finite element method (FEM) analyzes are conducted. It can be said that the natural frequencies are not suited well especially in high frequency ranges due to frequency dependent properties (visco-elastic) of PC.

ARTICLE INFO

Article history:
Received 27 November 2023
Revised 19 January 2024
Accepted 3 February 2024

Keywords:
Polymer concrete
Damping
Polyester
Resin
Modal
Vibration

1. Introduction

Polymer concrete (PC) has gained more importance in infrastructure industry as a powerful material for last decades. Due to its ability to be less labor-efficient and higher mechanical strength, higher chemical resistance then classical concrete, it is utilized for drainage channels, cable channels, even more machine tool bed. While the cement-based concretes have maximum 30–35 MPa compressive strength and 7–8 MPa flexural strength, polymer concretes have 90–100 MPa and 20–25 MPa respectively (Cakir 2022). Besides aggregates, polymer-based resin is combined with accelerator, hardener, maybe additives. In the industry, different types of resin are utilized such as epoxy, unsaturated polyester. Resin concrete is manufactured by blending a monomer or resin with aggregate, and subsequently polymerizing or curing the mixture. Among these materials, resin concrete, widely employed, utilizes matrix materials such as unsaturated polyester, epoxy, and acrylic resins, while pebble and sand serve as the aggregate materials for the resin concrete. By using different types of resin and aggregates ratios, one can hold different mechanical properties, as well as damping.

Damping in PC remains a subject of ongoing investigation among researchers, while the damping mechanism of real structures remains an incompletely resolved topic (Rasa and Özyazıcıoğlu 2021). Alterations in the damping ratio (DR) can be achieved by introducing fibers or combining different material types. Damping is attributed to phenomena occurring within the material grains, leading to energy loss. Factors such as grain

* *Corresponding author*. Tel.: +90-212-444-1-428 ; E-mail address: arifulu@aydin.edu.tr (A. Ulu)
ISSN: 2548-0928 / DOI: https://doi.org/10.20528/cjcrl.2024.02.002

boundary cracks, intragranular cracks, and interstitial voids in coarse solid aggregate contribute to increased energy dissipation, resulting in improved damping (Chinnuraj 2021). Various techniques, including damping ratio, loss factor, decay constant, and quality factor, are employed to assess the damping properties of materials. The study by Kim et al. (1995) explores mechanical properties by varying the size, compact ratio, and ingredient contents. A damping ratio of 1.3–1.4% is obtained for pebble content. Orak (2000) produces PC samples with a fixed 20% unsaturated polyester resin and different aggregate compositions, finding PC suitable for machine tool beds due to its viscoelastic nature. However, no correlation between filler composition and damping is identified. Cortes and Castillo (2007) compare epoxy resin polymer concrete (10%) with gray cast iron for machine tool applications, showing that PC has advantages in damping ratio (0.79–2.21%). Suh and Lee (2008) develop a machine tool bed polymer concrete with 10% polyester resin, yielding a DR between 2.93–5.69%. Bedi and Brar (2014) investigate the impact of polyester resin content (16–24% w.t) in PC on the loss factor using a DMA device, presenting equivalent damping ratios in Table 1.

Table 1. Summary of the literature about damping.

Literature	Resin type	Resin ratio (wt%)	Aggregate size	Aggregate+Filler	Damping ratio (%)	Method
Kim et al. (1995)	Epoxy	7.5	Mesh Size 6	Sand + Pebble	1.3–1.4	Log decrement
Li et al. (1996)	Epoxy	4.9*-13*	0.08-11.1mm	Granite + Rubber	2.18–2.67**	DMA
Orak (2000)	Polyester	20	0.25 – 8 mm	Sand + Quartz	1.66–2.86	Log decrement
Cortes and Castillo (2007)	Epoxy	10	0-10 mm	Basalt + Quartz	0.79–2.21	Log decrement
Suh and Lee (2008)	Polyester	10	Mesh Size 12	Sand	2.93–5.69	Half-power bandwidth
Bedi and Brar (2014)	Polyester	16-24	0.225-0.6 mm	Sand+$CaCO_3$	2.8–7.6 (20 Hz)** 2.74–7.28 (40 Hz)**	DMA
PC with additional materials						
Bignozzi et al. (2002)	Polyester	12	0.075-2 mm	Silica + $CaCO_3$ + Fibers	Varying with temperature	DMA
Jeon et al. (2015)	Epoxy	20	0.25-1.2 mm	Unknown + Carbon Fiber	0.75–1.0**	
Hwang et al. (2019)	Epoxy	20-30	0.25-1.2 mm	Sand + Recycled PEI	0.8–1.0**	Half-power bandwidth
Trancossi et al. (2022)				EPUMENT 140 Series	0.46–0.99**	Half-power bandwidth
Bai et al. (2009)	Epoxy	8-16	0-10 mm	Granite proportion + Glass Fiber	0.16–0.33	Half-power bandwidth
Damping studies of cement concrete						
	Concrete Type		Aggregate size	Fiber of filler	Damping ratio (%)	Method
Mo et al. (2020)	C30		Max 20 mm	PP fiber & Rubber powder (380μm)	2.64–4.72	Log decrement
Li and Xiao (2021)	C30		Max 25 mm	Recycled Aggregates	3.1–4.6	Half-power bandwidth
Li et al. (2021)	New to old concrete		Max 25 mm	Recycled Aggregates	6.0–8.0	Half-power bandwidth
Xi et al. (2021)	UHPC		Fine modulus 2.5	Steel Fiber	2.7–3.7	Half-power bandwidth & Log decrement

* Volume percentage

** Calculated equivalent damping ratio

Research on the DR effectiveness of different materials on pure PC is found in the literature, including recycled materials or fibers. Jeon et al. (2015) use epoxy resin (20%) with carbon fibers for railway slab noise, concluding that the loss factor increases with the weight percentage of fibers, with fiber PC having a 4dB advantage in noise reduction compared to PC alone. Hwang et al. (2019) address railway-induced slab noise mitigation using recycled polyetherimide (PEI), finding no significant variation in dynamic characteristics concerning the weight percentage of epoxy resin (20–30%). Therefore, they study variations in PEI content to enhance damping performance. Troncossi et al. (2022) aim to enhance the damping capacity of machine beds using EPUMENT 140

polymer concrete, calculating the damping ratio of pure PC content through modal analysis.

Besides damping studies of PC, it has also been investigated damping of traditional concrete by utilizing fibers, fillers, nano-tubes etc. It is stated in the research of Chi et al. (2019), controlling the filler effect in cement matrix composites involves managing the particle size and volume fraction of the inorganic powders. The presence of multiple phase boundaries and interfaces between nanotubes and the cement matrix increases the likelihood of interfacial slippage, leading to elevated energy dissipation, as well. In the results of Mo et al. (2020), it is found that addition of rubber powder enhances damping capacity (2.64–4.72%) of polypropylene fiber reinforced concrete (PFRC) but comes at the cost of reduced compressive strength and an increase in peak strain within the concrete. Li and Xiao (2021) study employs free vibration attenuation as a method to assess the damping characteristics (3.1–4.6%) of recycled concrete at varying rates of recycled aggregate replacement. Li et al. (2021) research investigates the impact of the interface in recycled concrete on damping performance by examining specimens comprising bonded new and old concrete. The study utilizes semi-precast concrete specimens incorporating both old and new concrete. The damping ratio falls within the range of 0.005 to 0.007 at high-frequency positions and 0.06 to 0.08 at low-frequency positions. Xi et al. (2021) explored four damping testing techniques (T-type method, cantilever beam method, simply supported beam method, and suspension method), three analytical approaches (half-power bandwidth method, INV damper method, time-domain method), and examined the impact of sampling frequencies on damping results.

Given damping studies in this paper are tabulated in Table 1. As seen in the literature, determining DR of PC with respect to resin ratio is an attractive content. In this regard, polyester resin ratio effect on damping issue is investigated. In this paper, PC specimens with resin ratios of 11–19% are prepared, the specimens are fixed to the experimental setup to conduct modal testing. Samples of polymer concrete are fixed at one end, then it is subjected to excitation using a hammer. Vibration data is acquired using a data logger and later processed with the 'Signal Processing Toolbox' of Matlab. The experimental Frequency Response Function (FRF) responses are analyzed to determine the stable modes and damping. Lastly, calculated damping ratios of beams are listed.

2. Materials and Method

PC samples are prepared in the polymer concrete channel factory of Mert Casting Inc company. Unsaturated polyester resin (UPR) is available on market, and it is selected as binder due to its lower cost comparing to epoxy resin. General purpose resin, details given Table 2, can wet fillers well. UPRs are thermosetting and can solidify from a liquid under the certain conditions. The main polymer chain of this resin has ester bonds, which are created by the compression of a multifactorial alcohol compound and its multifactorial acid.

Granulometry of silica-sand aggregates (Fig. 1), density 2.6 g/cc with 0.1–3.15 mm grain size, are adjusted according to Fuller curve and its chemical composition is given in Table 3. Sample recipes cannot be shown here due to company restrictions.

Table 2. Technical properties of resin (Cakir 2022).

Properties	Values
Flexural strength in 5% strain (MPa)	51.6
Compressive strength (MPa)	34.1
Impact strength (J/m)	12.9
Viscosity (mPa.s)	659
Shore hardness	80
Tensile modulus (MPa)	527
Density (g/cm^3)	1.225

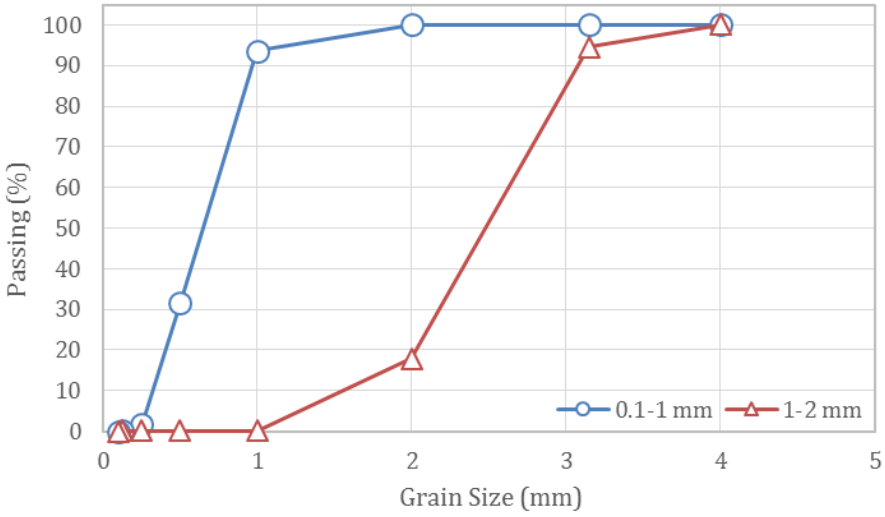

Fig. 1. Grain size distribution of aggregates.

Table 3. Chemical compositions of aggregates.

Chemicals	Aggregates		
	0.1–1 mm	1–2 mm	2–3.15 mm
MgO (%)	0.10	0.06	0.06
Al_2O_3 (%)	0.245	1.86	1.86
SiO_2 (%)	98.86	94.15	94.15
CaO (%)	0.01	0.39	0.39
Fe_2O_3 (%)	0.148	0.46	0.46
SO_3 (%)	-	0.10	0.10
K_2O (%)	0.03	1.56	1.56
Na_2O (%)	0.02	1.12	1.12
Loss (%)	0.587	0.30	

Furhermore, Calsite ($CaCO_3$) and AAP (acetylacetone peroxide) is utilized for filler and hardener. AAP, a quick-setting peroxide that is often used to harden UPRs, was applied. Technical details of AAP are given in Table 4. Apart from the AAP, Methyl Ethyl Ketone Peroxide (MEKP) could also be chosen for hardener (Cakir et al. 2020).

In order to activate UPR in room temperature (20 °C), Cobalt naphthenate, whose technical specifications are tabulated in Table 5, was selected as AAP accelerator. Usually, accelerators increase the system's heat, which makes resin reactions quicker. All components in each mixture are added at a consistent weight ratio.

Prior to use, all aggregates are thoroughly cleaned with water to prevent any contamination. After the aggregates are prepared, they are filled into the production machine. Hardener and accelerator are added to the aggregate mixture that comes out of the device along with calcite and resin and filled into the molds as seen in Fig 2(a). According to grain size, samples dimensions are determined in 10x25x500 mm as seen in Fig. 2(c). As stated in Cakir (2022), PC achieve over 80% of their mechanical strength in the initial three days, and there is minimal alteration in their long-term strength beyond the seventh day. Therefore, all of the samples are utilized after fourteen days with curing at room temperature. Furthermore, the mixtures were made by machine and the amount of accelerator was increased specially only for this study. The mixture coming out homogeneously from the end of the machine was immediately poured into the molds. Thus, rapid curing was achieved, and precipitation formation was prevented.

Table 4. Technical properties of hardener (Cakir 2022).

Properties	Values
Flash point	> 60 °C
Density, 20 °C	1055 kg/m³
Viscosity, 20 °C	21 mPa.s
Self-accelerating decomposition temperature (SADT)	60 °C
Total active oxygen	4–4.2%
Peroxide content	33%
Diethylene glycol + water + diacetone alcohol	67%

Table 5. Technical properties of accelerator (Cakir 2022).

Properties	Values
Density (at 20 °C)	0.92 g/cm³
Viscosity (at 20 °C)	300 mPa.s
Self-accelerating decomposition temperature (SADT)	≥ 150 °C
Flash point	62 °C
Cobalt content	1.50%

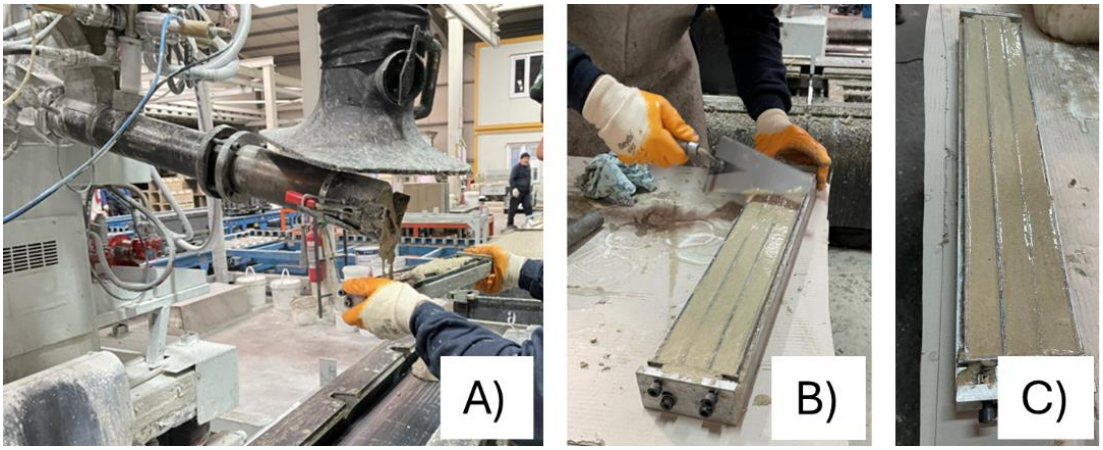

Fig. 2. Preparation of samples: (a) Filling the mold; (b) Flattening the surface; (c) Curing.

In the area of structural engineering, analyzing dynamic systems frequently focuses on two key components. Comprehending a system's natural frequency and damping ratios yields thorough understanding of its behavior. To avert possible harm, it is important to refrain from driving a system within the frequency range of 0.8 to 1.25 times its natural frequency. The natural frequencies of structures with established mass and stiffness may be computed or gauged using uncomplicated analytical techniques. Unlike natural frequency, determin-

ing the damping ratio is rather arduous and necessitates analytical assumptions. As a result, multiple damping models have been documented in the literature, representing the intricacy of this component.

These fundamental parameters can be determined through experimentation, even in the absence of an analytical model and specific structural or material details. Modal analysis, which is an experimental technique, is utilized to acquire the damping ratios and natural frequency of a system by observing the signal relationship between input and output. A hammer generates the input signal, allowing the system to become excited across all frequencies. The output signal of the system comprises the responses measured at specific points through accelerometers or displacement sensors. When there is a single input and one output channel, it is termed SISO (Single Input Single Output); whereas, if multiple input and output channels are involved, it is referred to as MIMO (Multiple Input Multiple Output).

Once the input/output signals have been obtained, it is essential to carry out a careful analysis, and in the event of unreal results, to repeat the experiments. The first step is to demonstrate a high correlation, called coherence, between the input and output signals. The coherence amplitude ranges from 0 to 1. Low values signify a weak correlation between input and output channels, which may be attributed to factors such as noise or gaps in the excitation spectrum at specific frequencies. Values approaching 1 indicate robust and representative measurements. Peaks observed in frequency-amplitude plots correspond directly to the natural frequencies of the system. In cases where multiple peaks are present, phase amplitude curves can be used. If there is instability around the natural frequencies, finite element programs or analytical models can be used. The stability diagram is a visual representation commonly illustrating the relationship between damping ratio and natural frequency for each mode in the examined structure. Its significance lies in validating the trustworthiness of modal analysis outcomes by pinpointing stable and accurate regions within the frequency-damping space for identified modes. Any instabilities or uncertainties concentrated around specific frequencies become apparent on the diagram. If a mode is situated within an unstable region, it could suggest problems like measurement noise, insufficient excitation, or numerical errors in the analytical process. In essence, the stability diagram is instrumental in assessing and enhancing the precision of modal analysis results in the realm of structural dynamics. By considering the above factors, the natural frequencies of the system can be accurately determined.

In the experimental arrangement, the molded samples were tied to a stable table by using a vice to adhere to the fixed boundary condition. The accelerometer was positioned at the end of the PC beam, as illustrated in the Fig. 3. However, the PC surface made it difficult to attach the accelerometer directly onto the rod. To resolve this problem, a plastic clamp (Fig. 3(a)) was utilized to fasten the accelerometer to the beam. Throughout the experiments, the accelerometer and the hammer were connected to a data acquisition system (Fig. 3(b)).

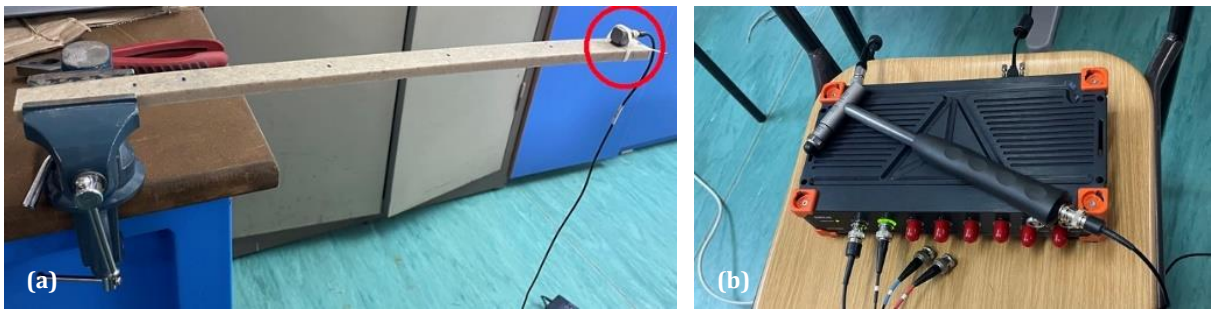

Fig. 3. Experimental Setup: (a) PC beam with accelerometer; (b)Data logger and impact hammer.

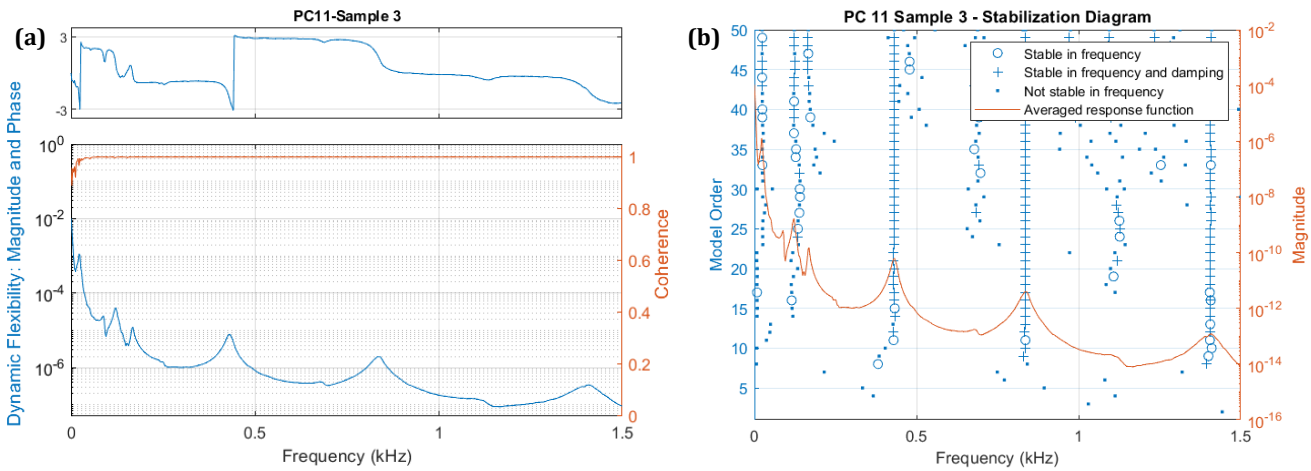

Fig. 4. Plots from modal testing: (a) Resonance, phase and coherence; (b) Evaluating frequencies and damping ratios.

The experimental procedures implemented the SIRIUS® HD-ACC data logger by Dewesoft, which can measure within the 0-20kHz range. The Kistler IEPE accelerometer has a sensitivity of 101.3 $mV.g^{-1}$ within the ±50g range. The IH-02 series from DJB Instruments acted as the actuator for the PC beam, exhibiting a 2.48 $mV.N^{-1}$ sensitivity.

3. Results and Discussion

Table 6 shows the four natural frequencies and four damping ratio values calculated in modal tests. For PC specimens, the number in the middle indicates the resin amount and S1, S2, S3 at the end indicates the number of specimens. Specimen PC_13_S3 could not be tested because it broke during transportation. Firstly, if the natural frequency results are analyzed; 1st natural frequencies were calculated as 24.36 Hz on average between 21.08-27.79 Hz. On the other hand, damping ratios were 6.12% on average and varied between 3.56-9.67%. The average, maximum and minimum values of other natural frequencies and damping ratios are given in the table. Fig. 5 is plotted by visualizing the damping ratios read from the table. Even in high frequencies, PC performs a good damping capacity considering other materials like gray cast iron (Orak 2000). As can be seen in the Fig. 5, a significant relationship was found between increasing the polyester ratio and the damping ratio until 17% polyester ratio. When 19% resin proportion is considered, an increment in the damping ratio is seen in Fig 5. Up to %17 resin ratio effects on the damping are plotted in Fig. 6. When samples with the same resin ratio are examined, the random distribution of the aggregates can vary the damping capacity. Even at 19% resin amount, the spread in the damping ratio was observed to be less than the other ratios. This showed that the effect of aggregate distribution was broken.

Table 6. Modal test results.

PC Names	1.Mode (Hz)	2.Mode (Hz)	3.Mode (Hz)	4.Mode (Hz)	DR_1 (%)	DR_2 (%)	DR_3 (%)	DR_4 (%)
PC_11_S1	23.66	123.17	457.66	890.42	6.44	3.94	1.94	1.95
PC_11_S2	24.95	121.96	476.27	918.64	5.57	3.95	2.00	1.75
PC_11_S3	23.53	121.68	430.97	835.92	8.75	3.94	1.98	2.00
PC_13_S1	25.49	183.54	485.85	940.28	4.59	1.92	1.93	1.91
PC_13_S2	27.79	125.30	539.06	1018.70	8.18	4.02	1.87	2.03
PC_13_S3	-	-	-	-	-	-	-	-
PC_15_S1	24.77	123.07	447.44	866.90	4.42	4.45	1.88	1.80
PC_15_S2	24.08	120.04	457.28	886.92	6.10	2.90	4.38	1.92
PC_15_S3	24.27	121.40	457.40	895.78	4.14	4.55	1.86	0.79
PC_17_S1	25.60	125.04	443.22	883.00	3.64	4.57	1.29	1.30
PC_17_S2	24.46	120.22	440.27	864.60	3.56	2.63	2.27	3.28
PC_17_S3	26.23	125.59	460.81	894.59	4.89	5.29	1.99	1.43
PC_19_S1	21.08	121.51	428.78	836.48	7.86	3.36	1.55	1.53
PC_19_S2	23.43	123.29	441.03	860.08	7.85	4.26	1.83	1.65
PC_19_S3	21.63	119.95	387.66	756.84	9.67	4.55	2.10	3.12
Minimum	21.08	119.95	387.66	756.84	3.56	1.92	1.29	0.79
Maximum	27.79	183.54	539.06	1018.70	9.67	5.29	4.38	3.28
Mean	24.36	126.84	453.84	882.08	6.12	3.88	2.06	1.89

Compared to the studies on pure PC, resin has the greatest contribution on damping capacity, while fine aggregate and filler have the least factor (Bedi and Brar 2014). Moreover, an increment trend in damping is seen until 20% resin proportion by considering maximum 0.6 mm grain size. Orak (2000) indicates that it remains uncertain whether the damping properties of polymer concrete vary based on the filler composition that is maximum 5mm grain size. The effect of resin amount on PC damping is not investigated due to constant at 20%. On the other hand, it is found that the granite proportion, which has maximum 10 mm grain size, is the most significant factor on the glass fiber reinforced PC (GFRPC) in the study of Bai et al. (2009), while the glass fiber dos-

age has the least impact on the damping ratio. Furthermore, it is mentioned that raising the epoxy dosage leads to a higher damping GFRPC, as the damping ratio of epoxy resin surpasses that of granite particles. As can be seen from the literature, the amount of resin is the most effective factor when using fine aggregates (0.6mm), whereas the grain size is the most effective factor when using coarse aggregates (10mm). In the study using 0-5mm aggregate, no significant relationship is found between aggregate size and damping capacity when the resin ratio is kept constant. In general terms, it can be said that even in the worst case, PC has a damping ratio even higher than that of cement-based concrete with admixtures (Mo et al. 2020; Xi et al. 2021).

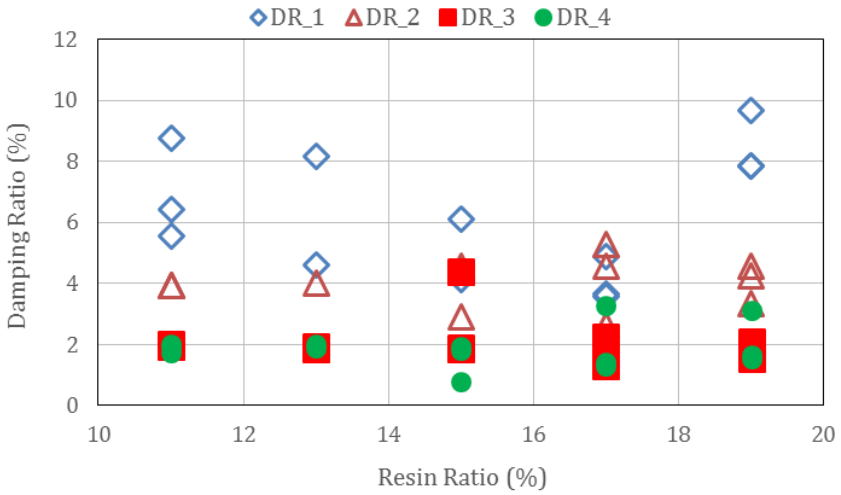

Fig. 5. Comparison of damping ratios.

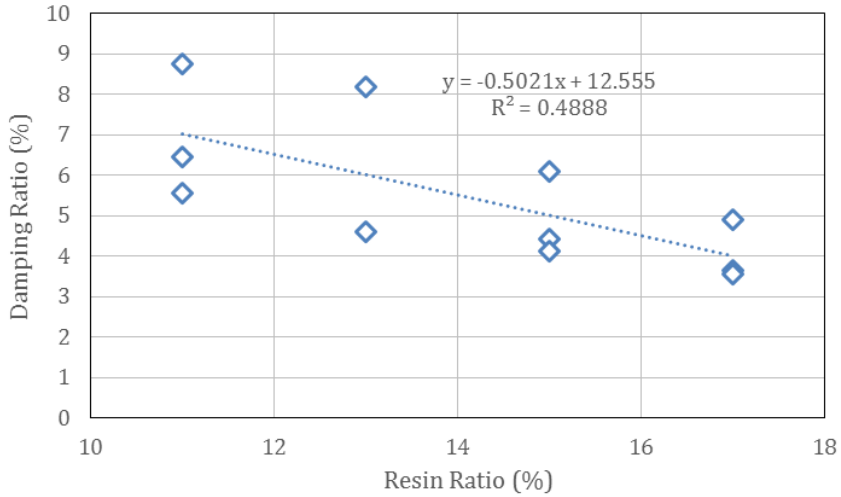

Fig. 6. Deviation of first damping ratios up to 17% resin amount.

Moreover, FEM analyses were performed for PC11 series to show the consistency of the experiments in ANSYS. The modulus of elasticity was taken as 17 GPa, Poisson's ratio as 0.18, density as 2150 kg/m^3. Based on PC11_S1 coded mixture, experimental and FEM results were compared in Table 7, while the first to fourth mode shapes were shown in Fig. 7. When the table was analyzed, inconsistency was observed in other modes except the first natural frequency. The difference between results were calculated between 11.50–16.10%. The reason for this is that the resin and therefore the polymer concrete shows visco-elastic properties. In other words, the modulus of elasticity varies depending on the frequency.

Table 7. Comparison of the results of PC11_S1.

Method	1.Mode (Hz)	2.Mode (Hz)	3.Mode (Hz)	4.Mode (Hz)
FEM	23.48	146.8	409.59	798.57
Experimental	23.66	123.17	457.66	890.42
Difference	0.77%	16.10%	11.74%	11.50%

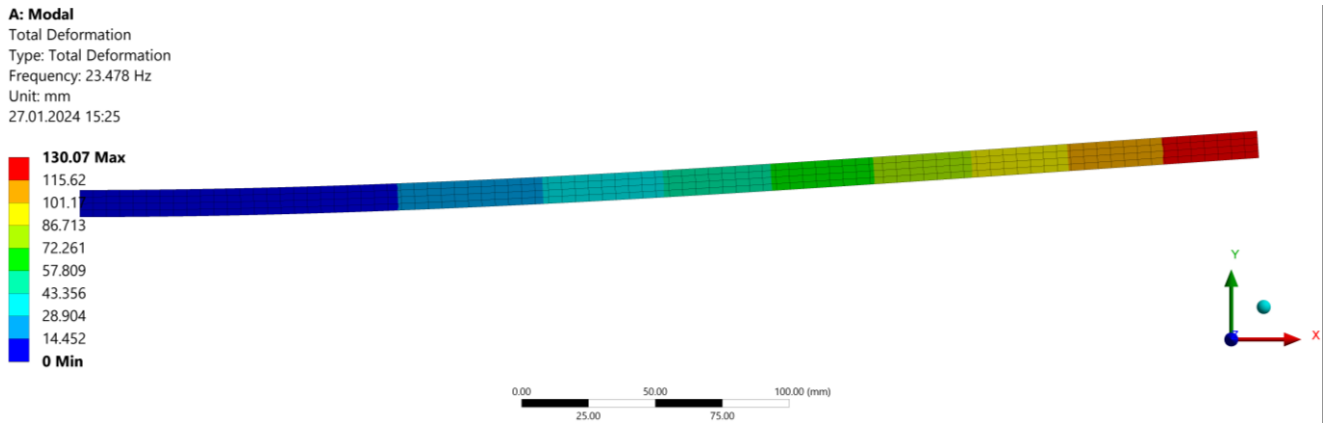

a) First Mode

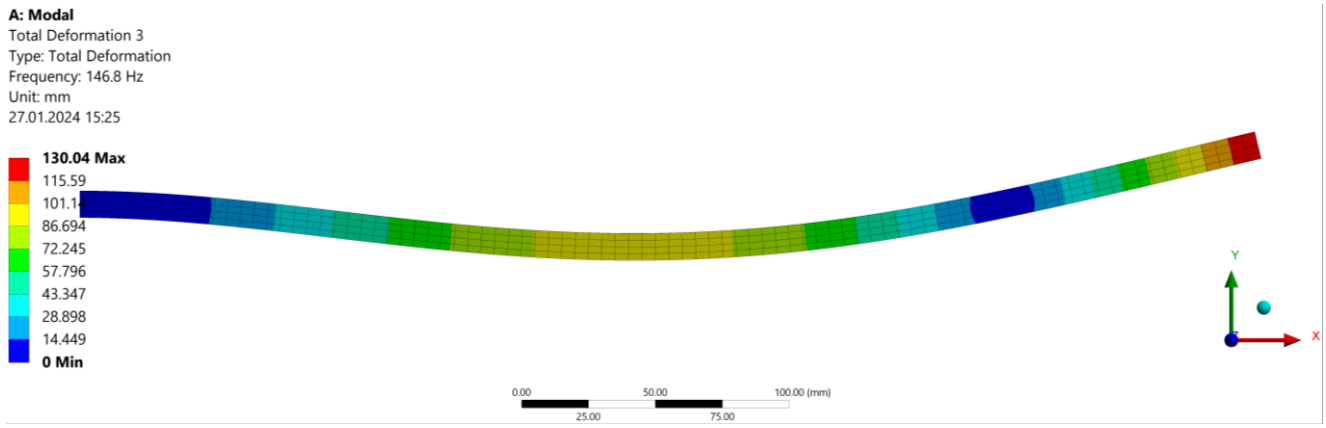

b) Second Mode

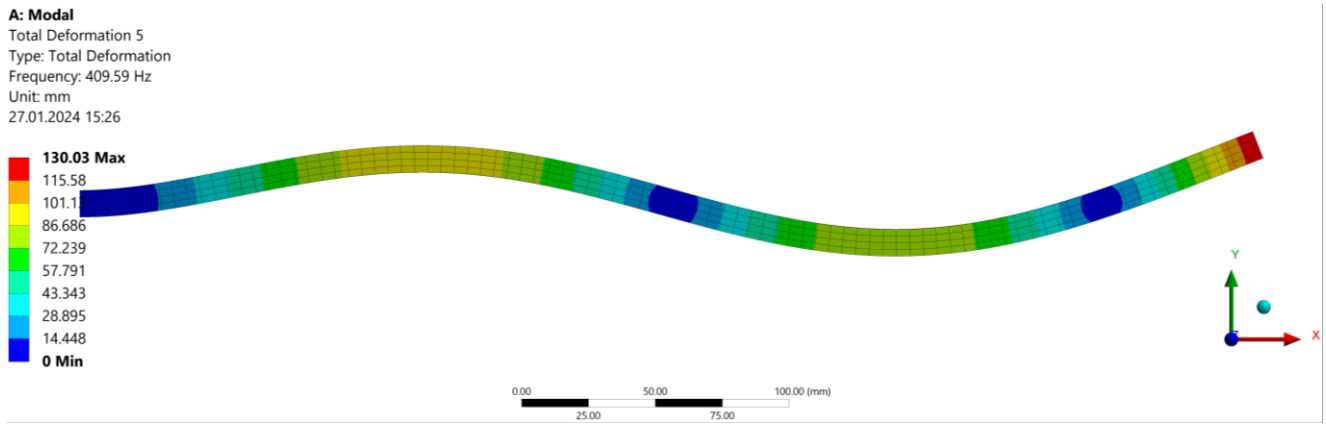

c) Third Mode

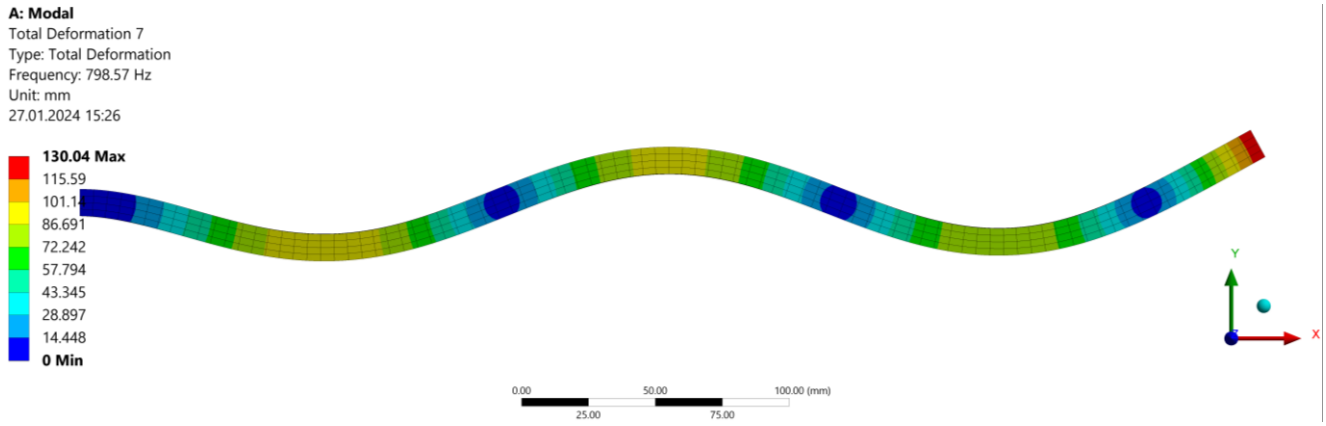

d) Fourth Mode

Fig. 7. FEM mode shape results of PC11_S1.

4. Conclusions

In this study, the effect of polyester resin amount on PC damping ratio was investigated. Aggregate sizes up to 3.15 mm were used and specimens were prepared by increasing the resin ratio and decreasing the coarse aggregate ratio. The specimens, which were fixed to the rigid table by providing the fixed-free boundary condition, were excited with a modal hammer, and the modal frequency and damping ratios were calculated with the help of Matlab software. When the results were analyzed, while the resin ratio increased up to 17%, the first damping ratio decreased and an increase of 19% resin ratio was recorded. However, when the same resin ratio samples were analyzed, it was found that the damping ratio was highly variable and that the randomly distributed sand grains were effective in determining the damping ratio. The least spread in damping capacity was observed at 19% resin content, due to low random aggregates distribution. Opposite to the literature, a negative correlation was obtained between damping ratio and resin amount. Because existing production recipe lists were used in production instead of certain experimental design methods. If the resin ratio increases in daily production, segregation begins, and fluidity increases. Therefore, leakages occur in the molds and the mixture is not distributed homogeneously in the products. The filler ratio is increased to reduce fluidity, prevent leakages, and prevent segregation. Another remarkable result is that the natural frequencies and FEM results are different. It was observed that the discrepancy of the results at high frequencies increased due to the visco-elastic properties of polymer concrete. In further studies the effects of coarse, fine, calcite and resin on the damping capacity of PC can be investigated by means of a design of experiments (DoE). In addition, the effect of visco-elastic material properties on the dynamic behavior of PC can be investigated.

Acknowledgements

The author would like to thank Mert Casting Inc. from İstanbul, Türkiye and the esteemed staff of the company, especially Remzi Usta and Ahmet Galip Sarıyıldız for their continuous support during the study.

Funding

The author received no financial support for the research, authorship, and/or publication of this manuscript.

Conflict of Interest

The author declared no potential conflicts of interest with respect to the research, authorship, and/or publication of this manuscript.

Data Availability

The datasets created and/or analyzed during the current study are not publicly available, but are available from the corresponding author upon reasonable request.

REFERENCES

Bai W, Zhang J, Yan P, Wang X (2009). Study on vibration alleviating properties of glass fiber reinforced polymer concrete through orthogonal tests. *Materials and Design*, 30(4), 1417-1421.

Bedi R, Brar SK (2014). Damping studies on polymer concrete. *Journal of Vibration Engineering & Technologies*, 2(1), 47-52.

Bignozzi MC, Saccani A, Sandrolini F (2002). New polymer mortars containing polymeric wastes. Part 2. Dynamic mechanical and dielectric behaviour. *Composites: Part A*, 33, 205-211.

Cakir F (2022). Effect of curing time on polymer concrete strength. *Challenge Journal of Concrete Research Letters,* 13(2)*,* 54-61.

Cakir F, Yildirim P, Gündoğdu M (2020). Effect of catalysts amount on mechanical properties of polymer concrete. *Challenge Journal of Concrete Research Letters,* 11(3)*,* 46-52.

Chi L, Lu S, Yao Y (2019). Damping additives used in cement-matrix composites: A review. *Composites Part B*, 164, 26-36.

Chinnuraj S, Ramaswamy TP, Venkatachalam MP, Nataraj M, Murugan R, Selvakumar M, Dhandabani S, ManojKumar KN (2021). Optimization of process parameters of epoxy granite for strength and damping characteristics using TOPSIS method. *Journal of Testing and Evaluation,* 49(3), 1956-1975.

Cortes F, Castillo G (2007). Comparison between the dynamical properties of polymer concrete and grey cast iron for machine tool applications*. Materials and Design*, 28, 1461-1466.

Hwang YT, Ahn SK, Koh HI, Park J, Kim HS (2019). Evaluation of mechanical/dynamic properties of polyetherimide recycled polymer concrete for reducing rail slab noise. *Functional Composites and Structures*, 1, 025002.

Jeon EB, Ahn S, Lee IG, Koh HI, Park J, Kim HS (2015). Investigation of mechanical-dynamic properties of carbon fiber reinforced polymer concrete for low noise railway slab. *Composite Structures*, 134, 27-35.

Kim HS, Park KY, Lee DG (1995). A study on the epoxy resin concrete for the ultra-precision machine tool bed. *Journal of Materials Processing Technology*, 48, 649-655.

Li S, Hu J, Song F, Wang X (1996). Influence of interface modification and phase separation on damping properties of epoxy concrete. *Cement and Concrete Composites*, 18, 445-453.

Li T, Xiao J (2021). The damping property of damaged recycled aggregate concrete after loading. *Journal of Building Engineering*, 35, 102096.

Li T, Xiao J, Singh A (2021). Influence of new-to-old concrete interface on the damping behavior of recycled aggregate concrete. *Structural Concrete,* 22, 3109-3122.

Mo J, Zeng L, Liu Y, Ma L, Liu C, Xiang S, Cheng G (2020). Mechanical properties and damping capacity of polypropylene fiber reinforced concrete modified by rubber powder. *Construction and Building Materials*, 242, 118111.

Orak S (2000). Investigation of vibration damping on polymer concrete with polyester resin. *Cement and Concrete Research,* 30, 171-174.

Rasa A, Özyazıcıoğlu MH (2021). Determination of the exact mode frequencies of multi-storey structures by state-space method and a comparison with mode superposition method. *Challenge Journal of Structural Mechanics*, 7(1), 1-10.

Suh JD, Lee DG (2008). Design and manufacture of hybrid polymer concrete bed for high-speed CNC milling machine. *International Journal of Mechanics and Materials in Design*, 4, 113-121.

Troncossi M, Canella G, Vincenzi N (2022). Identification of polymer concrete damping properties. *Proceedings of the Institution of Mechanical Engineers, Part C: Journal of Mechanical Engineering Science,* 236(21), 10657-10666.

Xi Y, Wenhua Z, Yilin P, Wanting Z, Fenghao Y (2021). Comparative study on damping test methods of concrete materials. *Construction and Building Materials*, 300, 124367.

Challenge Journal of Concrete Research Letters

Research Article

Predicting compressive strength of AAC blocks through machine learning advancements

Ehsan Harirchian [a,*]

[a] *Institute of Structural Mechanics, Bauhaus-Universität Weimar, 99423 Weimar, Germany*

ABSTRACT

Determining the strength properties of Autoclaved Aerated Concrete (AAC) through conventional compression experiments is both time-consuming and costly. Using sophisticated Machine Learning (ML) algorithms to forecast concrete compressive strength can expedite time-consuming experimental procedures and reduce expenses. In this study, four ML models were proposed, including Random Forest (RF), Support Vector Regression (SVR), Linear Regression (LR), and Stochastic Gradient Descent (SGD). These models were developed to forecast the compressive strength of AAC blocks based on a dataset of 525 cubic samples. By comparing the results using different evaluation indices, the study analyzed each input variable's relative importance and impact on the output. The findings revealed that the SVR model had the least error and is thus the most suitable for concrete compressive strength estimation. This approach results in cost savings on both specimens and laboratory tests. Out of the seven input factors, which encompass the proportions of water, cement, sand, lime, fly ash, aluminum powder, and gypsum, the proportions of cement and water content were pinpointed as the most crucial characteristics. In contrast, aluminum powder and gypsum displayed less prominent significance.

ARTICLE INFO

Article history:
Received 2 January 2024
Revised 9 February 2024
Accepted 9 March 2024

Keywords:
Machine learning
Autoclaved aerated concrete
Compressive strength
Construction materials

1. Introduction

The construction industry plays a crucial role in driving the economy. As buildings and structures become more complex, climate change crises and new cities and districts emerge, producing sustainable building materials and structures becomes a significant aspect.

AAC is a well-known sustainable lightweight building material that has been widely used in the construction industry since its invention in Scandinavia over 70 years ago (Hamad 2014; Kalpana and Mohith 2020). However, accurately predicting its properties can take time and effort due to its intricate composition. AAC is a form of aerated concrete within a low-density cementitious product made of calcium silicate hydrates. The low density is achieved by forming macroscopic air bubbles, mainly through chemical reactions. The air bubbles are uniformly distributed and retained in the matrix during setting, curing, and subsequent hardening with high-pressure steam in an autoclave machine to make a homogeneous structure of macroscopic voids or cells (Schober 2011; Qu and Zhao 2017). Many factors and criteria affect the final quality of AAC, impacting the safety of structures and products built with it.

Nomenclature

AAC	Autoclaved Aerated Concrete
LR	Linear Regression
MAPE	Mean Absolute Percentage Error
ML	Machine Learning
MSE	Mean Square Error
PGA	Peak Greound Acceleration
RF	Random Forest
SGD	Stochastic Gradient Descent
SVR	Support Vector Regression

* *Corresponding author*. E-mail address: ehsan.harirchian@uni-weimar.de (E. Harirchian)
ISSN: 2548-0928 / DOI: https://doi.org/10.20528/cjcrl.2024.02.003

A comprehensive exploration of AAC's mechanical properties becomes indispensable to enhance the comprehension of design methodologies and the behavior of AAC elements when subjected to external loads. Among these properties, compressive strength holds the utmost importance, given its direct connection to the structural integrity and safety of the construction. It assumes a pivotal role in evaluating the structure's performance over its entire lifecycle.

The concrete mixture for AAC is a meticulous blend of cement, lime, sand, and a crucial expansion agent, often aluminum powder, which induces significant expansion and the creation of voids within the mix. These ingredients are distributed in a randomized manner within the concrete mix proportion. Concrete compressive strength is influenced by many factors, encompassing specimen size, interaction duration, water-cement ratio, aggregate distribution, and the quantity of expansion agent employed. This intricate array of variables makes precise prediction of concrete's compressive strength challenging. Cubic concrete specimens are typically formulated following specific mix proportions and subjected to a drying period. Subsequently, the concrete's compressive strength is gauged through the utilization of a compressive testing apparatus.

However, such a testing method is usually uneconomical, inefficient, time-consuming, and labor-intensive (Jiang et al. 2022). Ordinarily, achieving an optimal mix ratio for concrete of a desired strength necessitates numerous iterations and rigorous laboratory evaluations. This task is even more intricate when dealing with AAC concrete than conventional concrete. The process demands a heightened level of expertise and a profound understanding of the chemical and mechanical attributes of the constituents. Typically, a sequence of tests is undertaken to attain the desired concrete properties. Alternatively, if a client mandates a particular strength, a tailored mix can be formulated to meet their specifications. Hence, substantial time and costs could be conserved if an accurate mathematical estimation of compressive strength can be made before conducting compression tests.

The scientific novelty of this study lies in establishing new correlations between tangible experimental data and derived values. These correlations involve empirical associations that are crucial for understanding the relationships between input features. Specifically, this study explores how empirical associations contribute to predicting the compressive strength of AAC blocks using Machine Learning (ML) techniques. For this purpose, four ML estimators, such as SVR, SGD, RF, and LR, have been employed to perform the compressive strength assessment of AAC blocks. A comparative study of these ML approaches is conducted to demonstrate the efficiency of each technique and the influence of the data employed in the analysis. Consequently, the significant importance of this study, in contrast to existing literature, resides in formulating a unique methodology for forecasting AAC's compressive strength through ML techniques. This encompasses identifying appropriate parameters for the methodology and pinpointing the influential factors and criteria that impact the efficiency of the suggested approaches.

1.1. Concrete compressive strength estimation and ML approaches

In mechanics, compressive strength, also known as compression strength, refers to the ability of a material or structure to withstand loads that tend to reduce its size or volume (Krivenko 2020). Concrete compressive strength plays a vital role in determining the mechanical properties of concrete, as it determines a material's ability to withstand compressive forces without undergoing failure or deformation (Mylvaganam and Elakneswaran 2023). Determining concrete compressive strength requires lengthy laboratory tests (El-Mir et al. 2023). With the recent development of ML methods and digitalization, it is very common, rapid, and convenient to implement ML methods into the construction process at all stages, including quality control in the production of building materials and compressive strength of concrete (Dudukalov et al. 2021; Harirchian et al. 2020, 2021; Muhammad et al. 2021; Tosee et al. 2021; Islam et al. 2022). For instance, a study by Fan et al. (2020) estimated the compressive strength values of concrete using Support Vector Machines (SVM) based on the concrete components. Cakiroglu et al. (2022) used ML algorithms to predict the axial capacity of fiber-reinforced polymer concrete columns. In a study by Aydin et al. (2023), an attempt was made to provide a predictive model for alkali-activated concrete carbon emissions using a neural network model and metaheuristic optimization algorithms. In a new work by Liu et al. (2024) an explainable ML-model has been implemented to predict punching shear strength of fiber-reinforced concrete flat slabs.

Behnood and Golashfani (2020) used the decision tree method to estimate the compressive strength of waste-added concretes. Hadzima et al. (2019) also implemented an Artificial Neural Network (ANN) for compressive strength estimation of concrete made by partially or completely replacing natural aggregate with waste rubber. In other studies, ANN algorithms such as Levenberg–Marquardt, Bayesian regularization, and scaled conjugate gradient back-propagation have been used to predict the compressive strength of self-compacting concrete with recycled aggregate (de Prado-Gil et al. 2022). Cheng et al. (2012) studied the applicability of SVM in the strength prediction of high-performance concretes in their study. Ni and Wang (2000) utilized multi-layer feed-forward neural networks to predict the compressive strength of concrete. Their research demonstrated that this approach was practical and advantageous in accurately estimating concrete compressive strength.

In the study of Erdal (2013), the author compared the estimated compressive strength values obtained through the Decision Tree (DT) method with the actual compressive strength values. Güçlüer et al. (Güçlüer et al. 2021) have made a comparative investigation to estimate the compressive strength of concrete by using different ML methods, including ANN, DT, SVM and Linear Regression (LR) for concrete compressive strength estimation. They have determined that the DT algorithm had the least error and is performed as the most appropriate ML method for their study. In the research conducted by

Deshpande et al. (2014), they employed the ANN to estimate the compressive strength of concretes made from recycled aggregates.

Shah et al. (2022) applied Gene expression programming, ANN, M5P model tree algorithm, and random forest to estimate compressive strength, tensile strength, and flexural tensile strength of concrete with the addition of metakaolin as a partial replacement for cement. Faridmehr et al. (2021) conducted a study utilizing a hybrid model that combined ANN with bat algorithm to estimate self-compacting geopolymer concrete's plastic viscosity and compressive strength.

ML can also predict the best mix of raw materials, such as cement, sand, water, and other ingredients, based on cost, performance, and sustainability criteria. For example, Albuthabak et al. (2019) investigated the estimation of concrete compressive strength by modeling ultrasonic pulse velocity values and mixing ratios using ANN and SVM. Yang and Du (2015) made a model by ANN to predict the compressive strength of concrete cubic and the effect of size on it.

By implementing optimization and ML in concrete production, manufacturers can improve their operations' efficiency, quality, and sustainability while reducing costs and minimizing waste.

2. Investigations for AAC

AAC has several advantages in contrast to conventional concrete. Notably, it offers an enhanced strength to weight ratio, a reduced coefficient of thermal expansion, and effective sound insulation attributed to the presence of air voids within the aerated concrete structure (Qu and Zhao 2017). However, AAC is commonly perceived as a conventional material; a study of existing literature demonstrates that in recent times, only a few studies have been undertaken, indicating substantial potential for enhancing composition optimization, material characteristics, shrinkage control, thermal properties, and long-term durability.

In 2000, Narayanan and Ramamurthy (2000) conducted a systematic review of research studies focusing on the production and properties of AAC. They stated that the porosity significantly impacts the compressive strength of AAC, and the reduction in bulk density and the related increase in porosity generally cause a reduction in strength.

Różycka and Kotwica (2022) examined the viability of partially substituting lime with waste derived from the purification of flue gases resulting from the incineration of industrial residues in the manufacturing of AAC. A study by Wongkeo et al. (2012) explored the compressive strength, flexural strength, and thermal conductivity of autoclaved concrete blocks produced by utilizing bottom ash as a substitute for cement materials. Ramamurthy et al. (2009) conducted a comprehensive investigation that summarized various facets of foamed concrete, an advanced variation of AAC. Their research encompassed detailed insights into constituent materials, mix proportions, production techniques, and foamed concrete's fresh and hardened properties.

Certain investigations have explored the incorporation of recycled or alternative materials in the production of AAC. For example, Rafiza et al. (2022) delved into the physical and mechanical attributes of AAC blocks produced through the utilization of recycled AAC as a partial replacement for sand. Another study by Mehmannavaz et al. (2014) examined the combined impact of fly ash and palm oil fuel ash on the heat of hydration in aerated concrete.

The research literature on AAC is relatively limited, highlighting the need for further and more comprehensive studies in this area. Given the significance of AAC as a lightweight and versatile building material, its potential benefits in various construction applications are substantial. However, the need for in-depth investigations can hinder the full understanding and utilization of AAC's capabilities.

Expanding the body of knowledge through additional research is crucial for several reasons:

- A more extensive range of studies would allow for a deeper exploration of AAC's production methods, properties, and potential advancements. Understanding its structural performance, durability, and long-term behavior under different conditions is essential for optimizing its use in practical applications.
- A broader scope of research can lead to improved standards and guidelines for the manufacturing and implementing of AAC, ensuring that it meets or exceeds safety and quality requirements. It can also facilitate the identification of best practices and innovative techniques for sustainable construction, promoting environmentally friendly building solutions.
- A more robust research base can foster greater confidence among architects, engineers, and construction professionals in incorporating AAC into their projects. Understanding the material's limitations and capabilities would lead to more informed decisions, ultimately driving its broader adoption in the construction industry.

2.1. AAC material properties and production materials

The characteristics of AAC are influenced by many factors, including the type of raw materials used, the design of the mix proportions, autoclaving conditions, and how these factors are impacted by advancements in materials and equipment, as well as our evolving comprehension of the process. When embarking on the production of AAC, several essential materials come into action as below:

- Fly ash: Fly ash is a product of coal-fired power plants and is commonly used as one of the primary ingredients in AAC blocks. It acts as a filler material and provides improved thermal and acoustic insulation properties.
- Cement: Ordinary Portland Cement (OPC) or Portland Pozzolana Cement (PPC) is used as a binder to hold the AAC blocks' structure together. Cement reacts with water and lime to form calcium silicate hydrate, which gives the blocks their strength.

- Lime: Lime is added to the mixture to enhance the self-curing properties of AAC blocks and provide additional strength.
- Sand: Sand is used as a fine aggregate in the AAC block manufacturing process. It contributes to the block's density and helps in achieving a smooth surface finish.
- Gypsum: Gypsum is added to the mix to control the setting time of the AAC blocks. It prevents the blocks from setting too quickly and allows for better workability during production.
- Aluminum powder/paste: Aluminum powder or paste is a key component that reacts with lime and water to produce hydrogen gas. This gas creates the aerating effect, causing the AAC blocks to expand and become lightweight.
- Water: Water is used to mix all the ingredients and initiate the chemical reactions that lead to the formation of AAC blocks.

The manufacturing process involves mixing these materials thoroughly and pouring the mixture into molds. Once poured, the blocks are subjected to steam-curing in an autoclave to complete the chemical reactions and attain their final strength. As a result of hydrogen gas evolution, the aerating effect creates a porous structure, making AAC blocks lightweight and suitable for various construction applications.

The chemical reaction in AAC mix is known as the "hydration" process (Hamad 2014). It involves the reaction between the finely ground silica-rich material (usually fly ash or sand) and lime (calcium hydroxide) with water in the presence of a small amount of aluminum powder.

A step-by-step explanation of the chemical reaction in AAC mix are as below. In the equations, xH_2O represents the variable amount of water molecules in the calcium silicate hydrate compound, and (aq) denotes an aqueous solution.

- Lime and water: The first step is the reaction of lime ($Ca(OH)_2$) with water (H_2O) to form calcium hydroxide ($Ca(OH)_2$) in an aqueous solution as presented in Eq. (1):

$$Ca(OH)_2 + H_2O \rightarrow Ca(OH)_2(aq) \quad (1)$$

- Silica-rich material and lime: The calcium hydroxide reacts with the silica-rich material (fly ash or sand) to produce calcium silicate hydrates (CSH), which are the main binding agents responsible for the strength of AAC as illustrated in Eq. (2):

$$Ca(OH)_2(aq) + SiO_2 \rightarrow CaO \cdot SiO_2 \cdot xH_2O \quad (2)$$

- Aluminum powder: Aluminum powder is also added to the mix. During the mixing process, aluminum reacts with the alkaline environment created by the lime and water. This results in the formation of hydrogen gas (H_2) bubbles (Kavita and Tarjani 2016) as presented in Eq. (3):

$$6Al + 8Ca(OH)_2 + 12H_2O \rightarrow 8CaO \cdot SiO_2 \cdot xH_2O + 6H_2 \quad (3)$$

A study by Hamad (2014) investigated that the volume increase depends upon the quantity of aluminum powder to react with the calcium hydroxide in the mixture.

- Foaming: The hydrogen gas generated in the previous step causes the mixture to expand and create a foamy texture, introducing aeration into the mix. The hydrogen, which is lighter than air in weight, rises up and is replaced by an air bubble as the hydrogen bubble comes out of the material (Domingo 2008).
- Curing: After the initial mixing, the AAC mix is poured into molds and cured in an autoclave. The curing process involves subjecting the mix to high-pressure and high-temperature steam, further enhancing the chemical reactions. The curing process helps form additional calcium silicate hydrates, strengthening the AAC and enhancing its properties.

The final result of these chemical reactions is a lightweight cellular structure with a matrix of calcium silicate hydrates, which gives AAC its unique properties such as low density, high thermal insulation, and good mechanical strength.

As previously stated, compressive strength refers to a material's capacity to withstand failure in the form of cracks and fissures. It is determined by the maximum load a specimen can bear before breaking. One common approach to measuring the strength of concrete is using a mechanical machine. This test is a destructive method but offers precise information about concrete strength and is widely employed for this purpose. Typically, the compressive strength of AAC blocks falls within the range of 2 to 4 N/mm^2 (2000 to 4000 kPa or 290 to 580 psi).

Fig. 1 depicts the sequential procedures encompassing the blending of raw materials and the attainment of compressive strength for the AAC samples employed in this research. The methodology involved subjecting standard 15 cm-cube concrete test specimens to compressive strength tests subsequent to the curing phase.

The evaluation of concrete sample compressive strength adhered to the standards outlined in DIN EN 771-4 (2011) and DIN EN 772-1 (2016).

3. Methodology

For implementing an ML technique in the casting process, a certain amount of concrete compressive strength tests must be collected to train and test, in which the AAC concrete mixture components (e.g., cement, water, sand, lime, etc.) are set as the input data. In contrast, the output data will be compressive strength value. Fig. 2 presents the procedures to implement ML techniques regarding compressive strength prediction.

3.1. Dataset

The first stage in constructing an ML model involves choosing input data from a dataset. These input data, represented by independent variables or attributes, play a role in shaping the model's behavior. The ML model then demonstrates how the input data attributes can impact the eventual outcomes. Methodologies can be categorized into destructive and nondestructive approaches in determining AAC's compressive strength. In the context of this research, the concrete compressive strength

test was employed, which falls under the category of destructive methods. The cubes used for this study have a dimension of 150 x 150 x 150 mm (see Fig. 3), and measurements were made on 525 samples with different mix ratios. To assure the accuracy of each mixture proportion's estimation, 5 samples for each design were examined. The initial dataset was acquired through meticulous and comprehensive laboratory experimentation. This dataset was partitioned into two subsets: the training and testing sets. Each set contains numerous vectors representing the influencing factors and corresponding concrete compressive strength values.

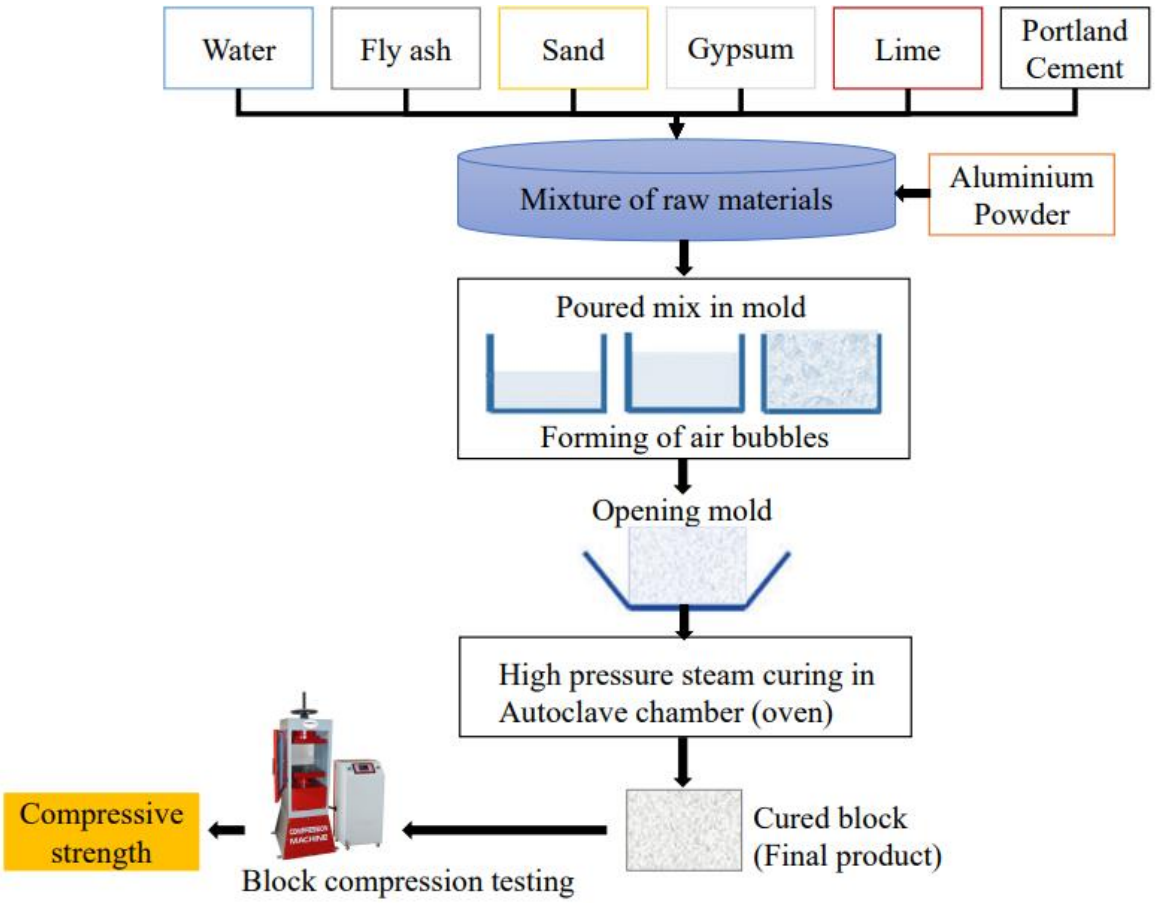

Fig. 1. Compressive strength of AAC block – Procedures from production to test.

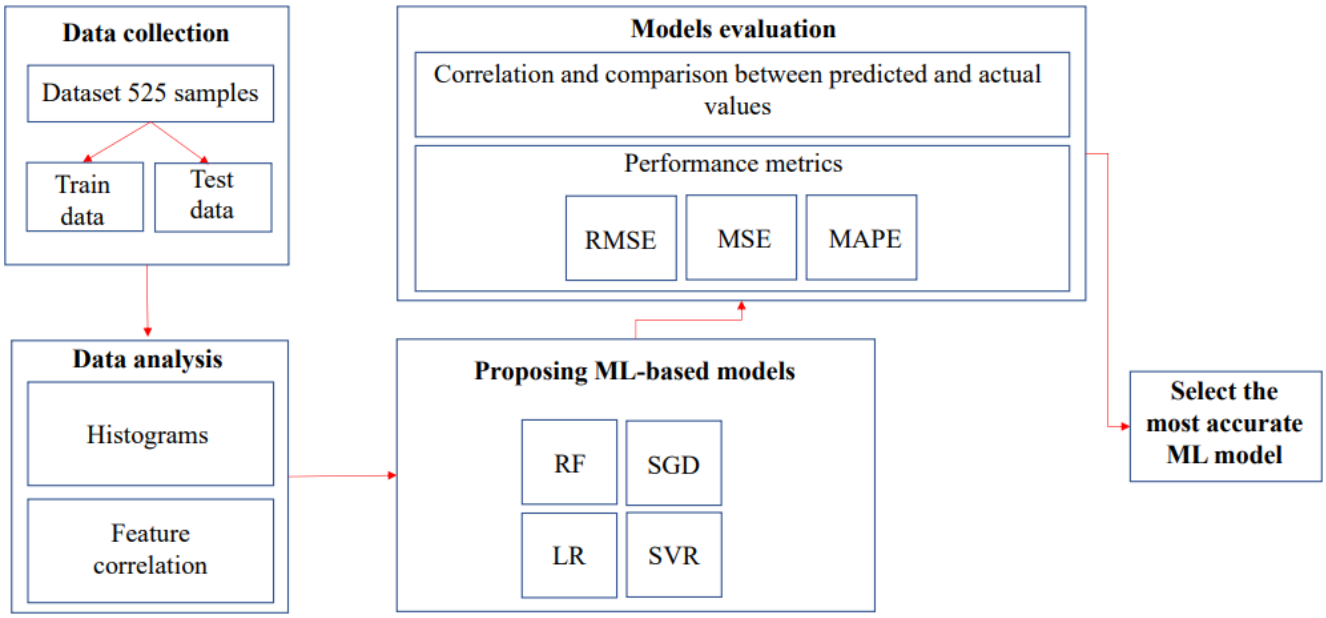

Fig. 2. Procedures to predict compressive strength of AAC block by ML.

Fig. 3. Some of the used AAC samples.

3.1.1. Input and output parameters

To evaluate the compressive strength of AAC blocks, it is required to gather basic proportional data. This data will help in understanding the relationship between different variables and the compressive strength of the blocks. During this study, the following data were considered:

- Block Dimensions: These dimensions can influence the compressive strength. The samples were 150 mm cubic.
- Composition: Various components of the AAC mixture, including cement, lime, sand, fly ash, aluminum powder, gypsum, and water, all contribute to its composition. The strength of the concrete can be influenced by the proportions of these constituents, and the following ranges represent the percentages of each material used.
  - Fly ash = 40 to 60 %
  - Cement = 10 to 20 %
  - Lime = 5 to 15 %
  - Sand = 10 to 25 %
  - Gypsum = 0.5 to 2.5 %
  - Aluminum powder = 0.5 to 3.5 %
  - Water = 20 to 40 %

The histogram depicted in Fig. 4 illustrates the distribution of input data. The *x*-axis represents the percentage of the material in the mix design, while the *y*-axis indicates the number of samples corresponding to each percentage.

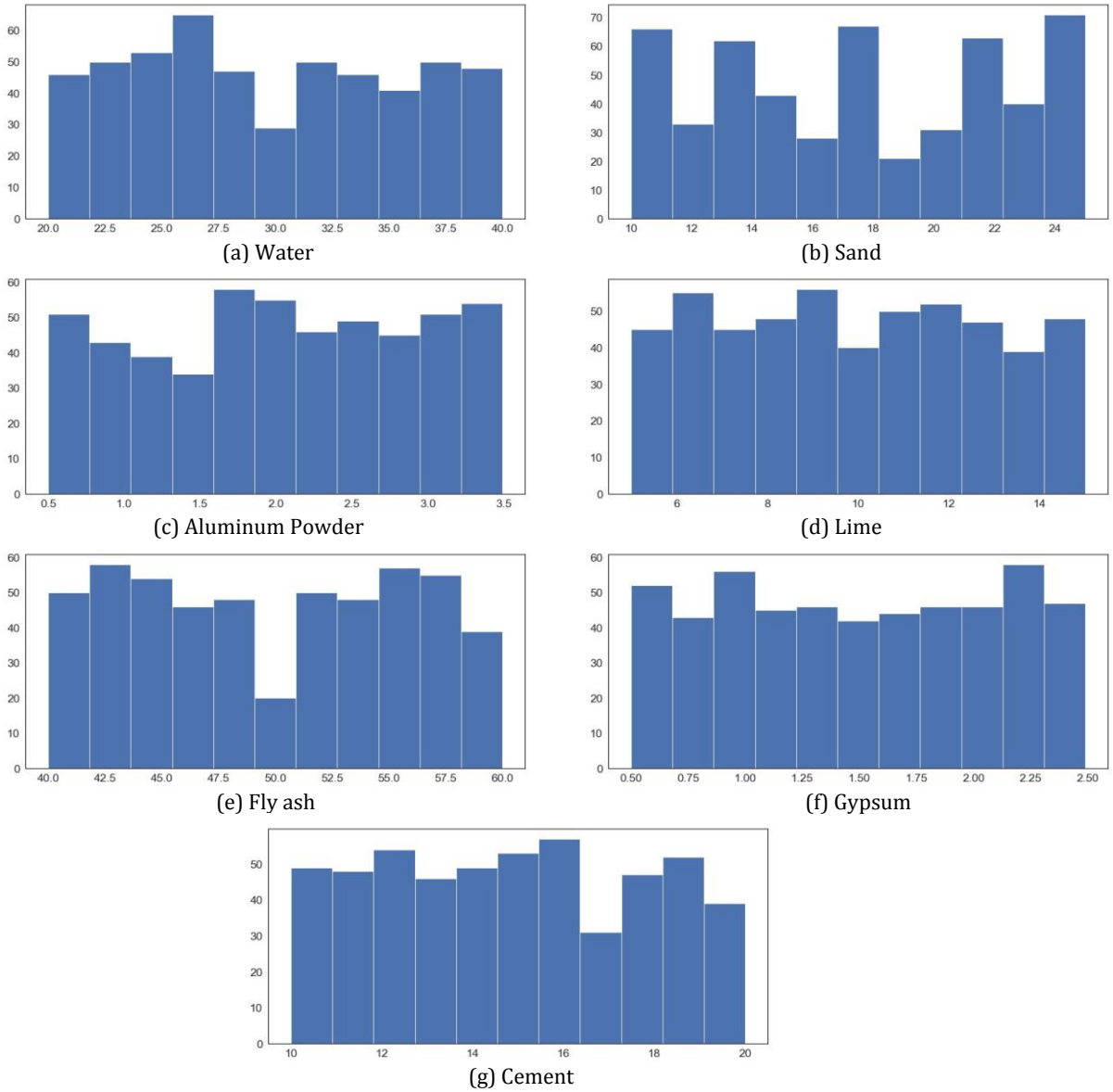

Fig. 4. Distribution of the entire experimental data.

- Curing Conditions: Every sample underwent a curing process lasting 12 hours within a laboratory autoclave chamber. This process took place at a temperature of 190°C and under a pressure of 12 bars. Following the curing process, compression tests were carried out on the blocks after they had cooled down naturally under ambient environmental conditions. These tests were conducted 48 hours after the cooling process within a temperature-controlled room.
- Number of Replicates: For each mix ratio there were 5 samples to conduct multiple tests to get representative and reliable data.

3.1.2. Splitting of dataset

The dataset has been split into two distinct groups: the training subset and the test subset. The typical approach is to allocate 80% of the data for training purposes and the remaining 20% for testing (Cohen et al. 2018; Korotcov et al. 2017). For this study, the same division was employed, using 420 data points for training and 105 data points for the test subset. The training set is comprised of data with known outputs, while the test subset is used to assess the model's predictive performance.

3.2. Model implementation

Four ML estimators have been applied using the Scikit-learn package and Python language. The fundamental analytical libraries required include Scikit-learn, Pandas, NumPy, and Matplotlib. The following sections describe selected ML estimators in brief.

3.2.1. Support vector regression (SVR)

SVR stands out as a potent and adaptable ML technique tailored for regression analysis, as outlined by Ger´on in" Hands-On Machine Learning with Scikit-Learn and TensorFlow" (Géron 2017). SVR identifies the hyperplane that best accommodates the data points within a higher-dimensional context. The core objective of SVR revolves around discovering a function capable of associating input data with continuous output values, all while minimizing the discrepancy between predicted and actual values. SVR proves its utility in managing intricate and non-linear connections between input and output variables. It achieves this by applying a kernel trick, which projects data into a feature space of higher dimensions. This technique notably shines when grappling with datasets characterized by high noise levels and a limited number of samples. In this study, the kernel type used for the SVR model was rbf.

3.2.2. Linear regression (LR)

LR holds a foundational status in the realm of ML, finding widespread application due to its capacity to elucidate the correlation between a dependent variable and one or multiple independent variables. The central mechanism entails fitting a straight line or hyperplane to a dataset, thereby enabling predictions of the dependent variable's values based on those of the independent variables. LR models are versatile tools, serving in both regression and classification tasks. Their appeal stems from their simplicity and interpretability, rendering them invaluable for exploratory analysis. Moreover, LR models often serve as foundational benchmarks against which more intricate algorithms are compared.

3.2.3. Random forest regressor (RF regressor)

RF regression, a variation of the RF algorithm, enhances prediction accuracy by aggregating the forecasts from numerous decision trees. This technique generates a collection of decision trees, each using randomly selected subsets of the training data and its corresponding features. The predictions of these individual trees are then averaged to yield the ultimate prediction. This strategy effectively mitigates overfitting, thereby bolstering model accuracy and its generalization capacity.

RF regression addresses linear and nonlinear relationships between input and output variables. This adaptability and applicability to datasets featuring many features mark RF regression as a versatile tool. Notably, the algorithm's interpretability and scalability contribute to its popularity as a preferred choice for real-world regression challenges. In this study, hyperparameter tuning by using GridSearchCV for RF Regression models has been performed to find the best combination of hyperparameters.

3.2.4. Stochastic gradient descent (SGD)

SGD regressor is a regression analysis technique geared towards refining model accuracy by minimizing the disparity between predicted and actual values by optimizing a cost function. This approach is a variant of the gradient descent algorithm, which takes a stochastic path to update model parameters. This stochastic approach involves computing the cost function's gradient on the training data's small, randomly chosen subsets. By employing this method, the SGD regressor aims to enhance the convergence rate while reducing computational expenses compared to the traditional batch gradient descent. This is particularly beneficial when dealing with substantial datasets featuring many features, where the computational burden of conventional batch gradient descent becomes impractical.

The SGD regressor demonstrates its utility in scenarios characterized by noisy data. It exhibits robustness and effectively handles linear and nonlinear connections between input and output variables.

3.3. Evaluate regression model

Within the context of evaluating ML regression models, it relies on metrics such as Mean MSE, Coefficient of Determination (R^2) and Mean Absolute Percentage Error (MAPE). In this case, smaller values are indicative of better performance. Hence, the model exhibiting the lowest metrics values will be deemed superior. These metrics offer insights into the precision of predictions produced by ML models and quantify the extent of deviation from actual values.

MSE calculates the squared difference between the actual and predicted values as presented in Eq. (4).

$$MSE = \frac{1}{n}\sum_{i=1}^{n}(y_i - \hat{y})^2 \quad (4)$$

where, n is the total number of samples, y and $\hat{y}$ are the actual values and predicted output values, respectively.

The coefficient of determination, also known as R^2, is a metric indicating the quality of fit for a model. In regression analysis, it gauges the extent to which the regression line accurately represents the observed data as presented in Eq. (5). This metric holds significance in predictive modeling and hypothesis testing within statistical analysis.

$$R^2 = 1 - \frac{\sum(y_i - \hat{y}_i)^2}{\sum(y_i - \hat{y})^2} \quad (5)$$

MAPE, functions as a gauge of the predictive accuracy inherent in statistical forecasting methods. This metric commonly quantifies accuracy through a ratio, as defined by Eq. (6).

$$MAPE = \frac{1}{n}\sum_{i=1}^{n}\left|\frac{y_i - \hat{y}}{y_i}\right| \quad (6)$$

where, y and $\hat{y}$ are the actual values and predicted output values, respectively. Their difference is divided by the actual value y. The absolute value of this ratio is summed for every predicted point in time and divided by the number of fitted points n.

4. Results and Discussion

4.1. Feature correlation

Gaining insights into the significance of features and understanding their correlations are pivotal during the construction of an ML model. This knowledge aids in identifying the optimal set of features, which in turn facilitates the creation of well-optimized models for the phenomena under investigation. Correlation, a measure of the linear association between variables, plays a key role in this process. The Pearson correlation of the dataset's inputs and output is visually depicted in Fig. 5.

In Fig. 6, it becomes evident that the percentages of cement and water in the mixture carry more significance compared to the other features. The vertical axis on this graph represents F-values, computed from the correlation values illustrated in Fig. 5. For a clearer interpretation, Table 1 provides the ranking of correlations based on their corresponding feature scores.

4.2. Prediction by ML

The dataset has undergone analysis using four distinct ML regressors, encompassing both training and testing data sets. Figs. 7–10 exhibit a visual representation of the actual and forecasted compressive strength values for the training data. Correspondingly, Figs. 11–14 demonstrate the same comparison for the testing data. These figures depict the results obtained from the SVR, LR, RF, and SGD regression models, respectively. The findings of this study suggest a favorable outcome from the employed ML estimators, showcasing the prediction accuracy by demonstrating a strong alignment between predicted and actual values. The application of advanced algorithms and intricate statistical methods has facilitated the creation of precise predictive models. These models effectively consider intricate variables and interconnected elements, contributing to the overall accuracy and reliability of the predictions.

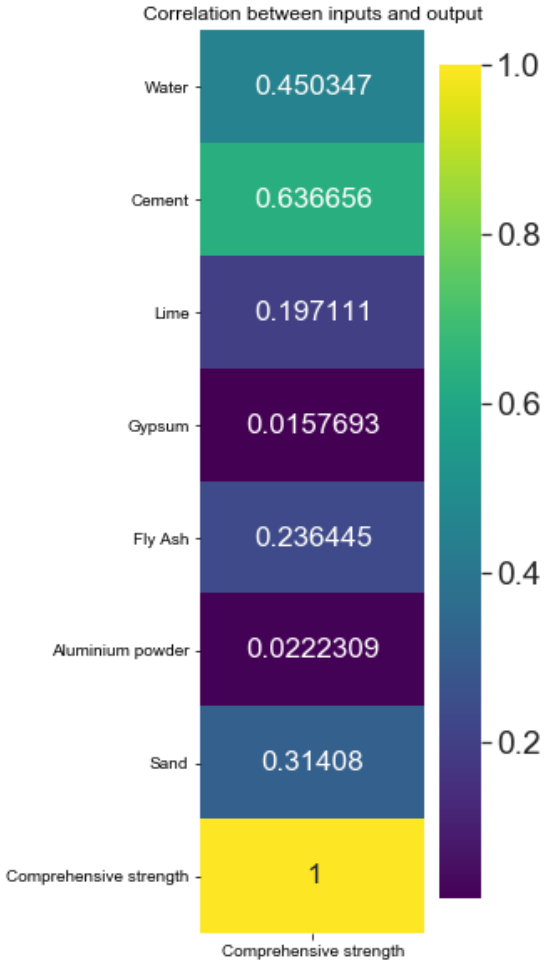

Fig. 5. Correlation between inputs and output.

Table 1. Sorting most correlated features to the output and the feature F-values.

Rank	Feature	F-Value
1	Cement	278.5
2	Water	97.01
3	Sand	33.13
4	Fly ash	27.43
5	Lime	24.01
6	Gypsum	12.82
7	Aluminum powder	9.34

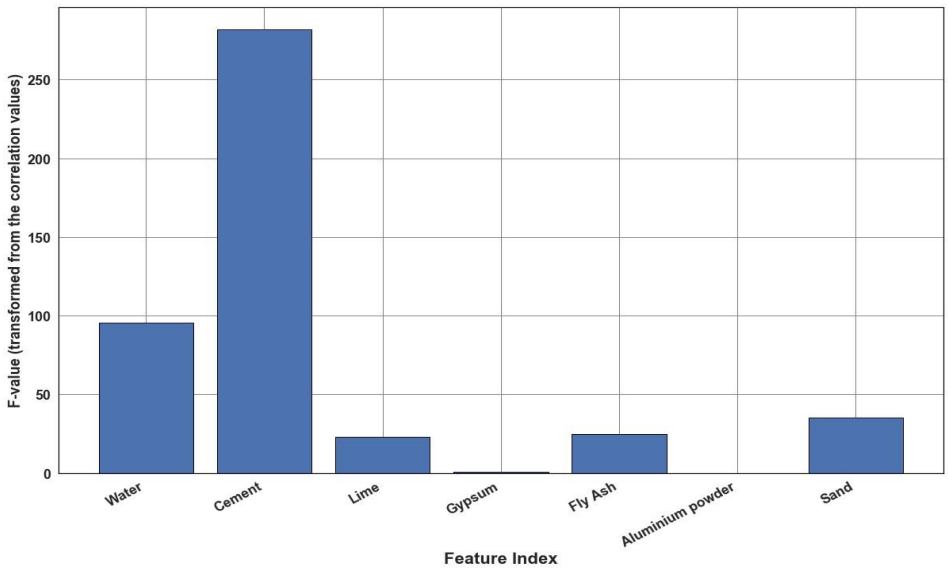

Fig. 6. Feature index.

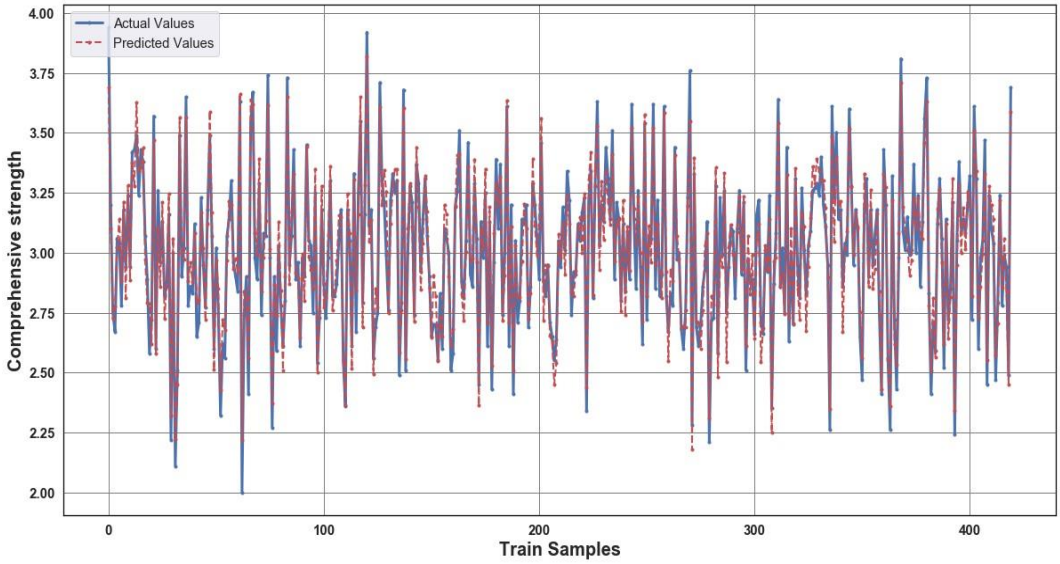

Fig. 7. Actual and predicted values by SVR for train data.

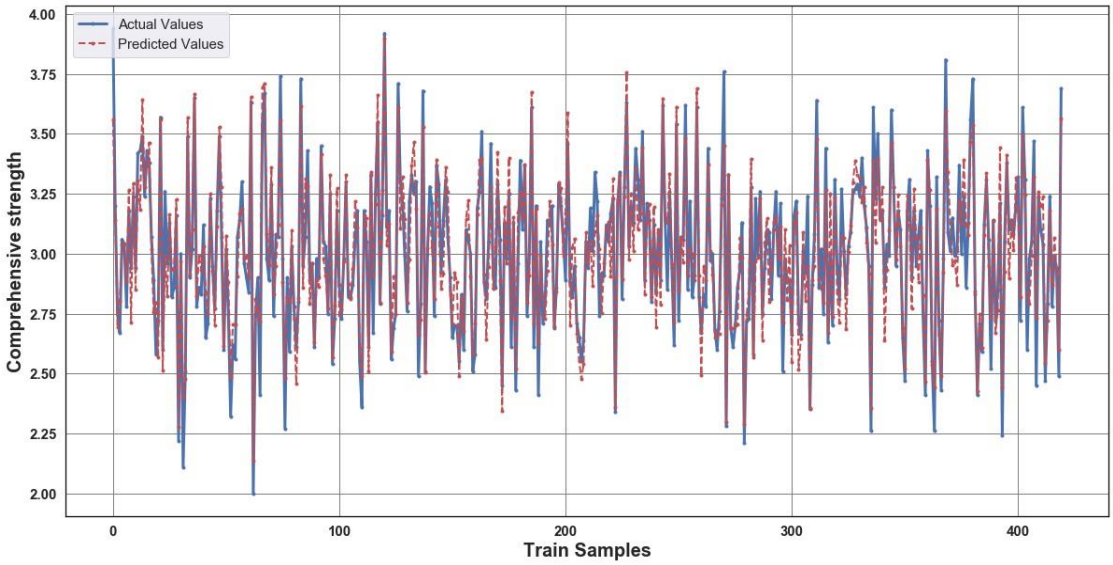

Fig. 8. Actual and predicted values by LR for train data.

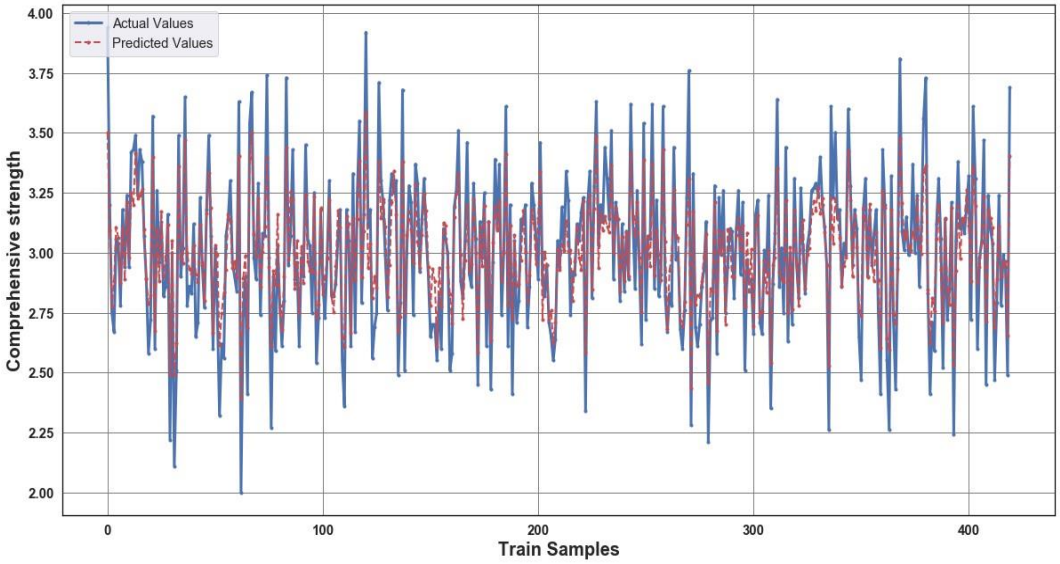

Fig. 9. Actual and predicted values by RF for train data.

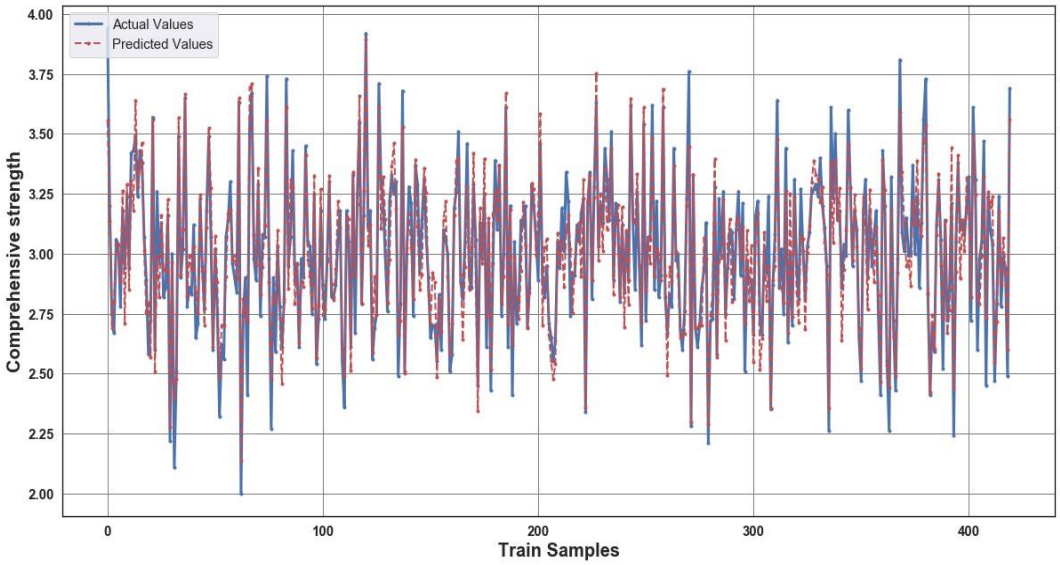

Fig. 10. Actual and predicted values by SGD for train data.

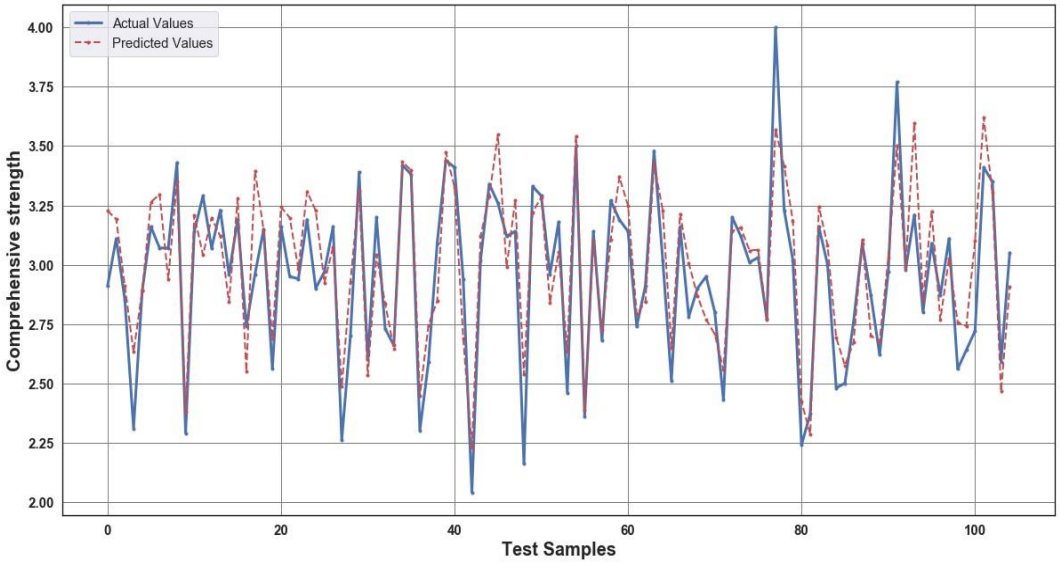

Fig. 11. Actual and predicted values by SVR for test data.

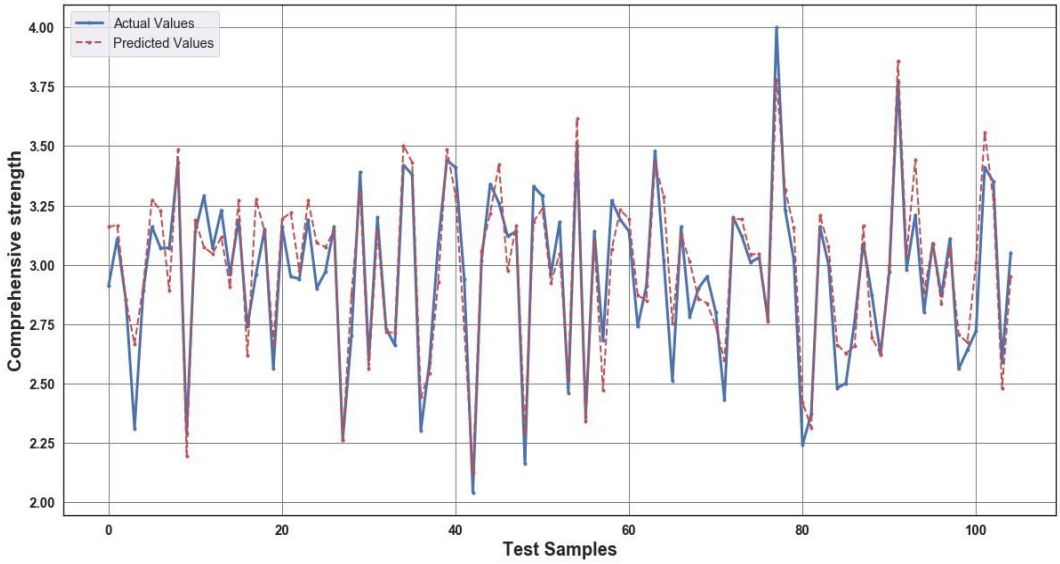

Fig. 12. Actual and predicted values by LR for test data.

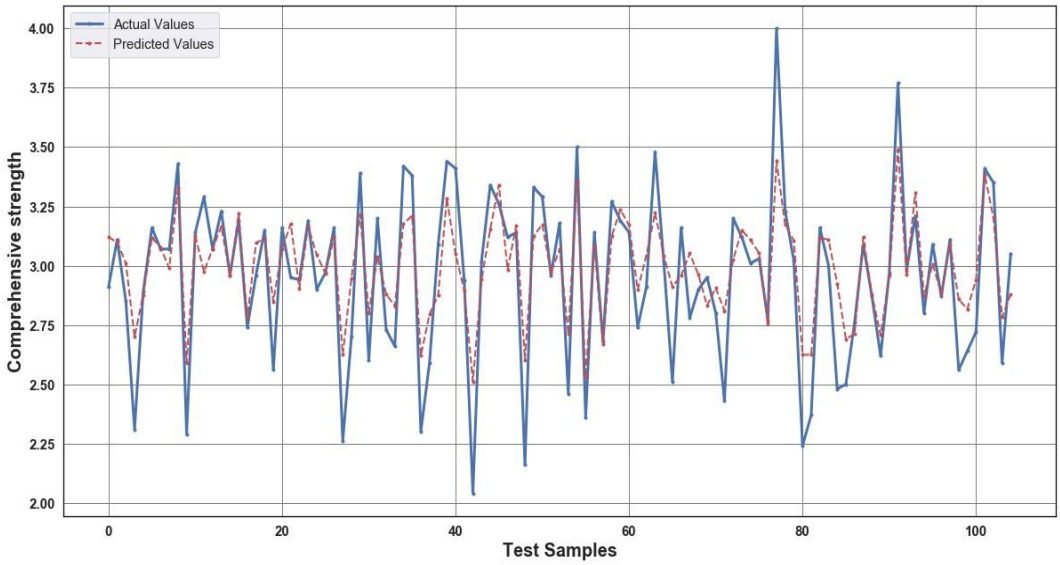

Fig. 13. Actual and predicted values by RF for test data.

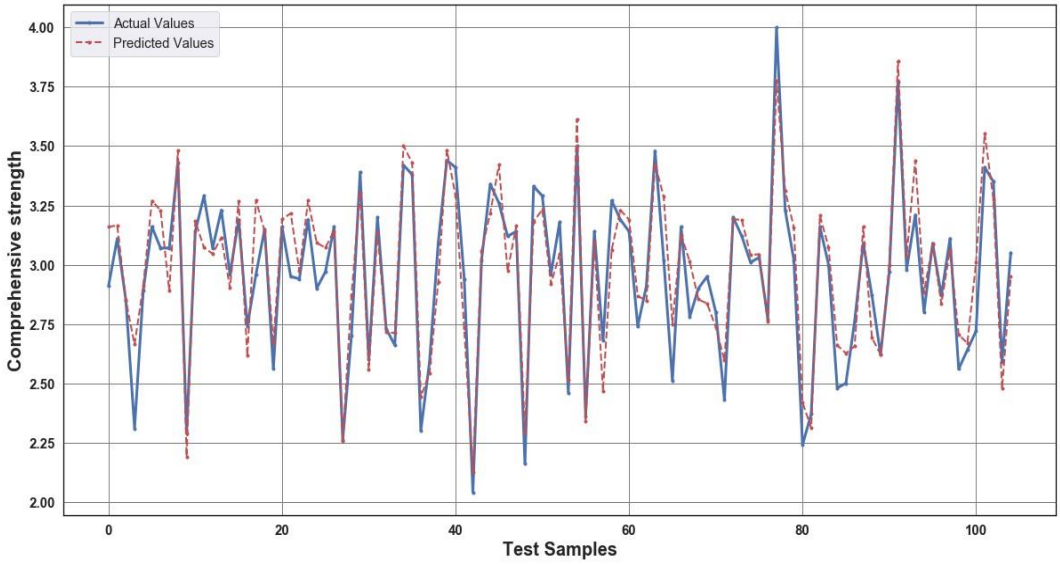

Fig. 14. Actual and predicted values by SGD for test data.

4.2.1. Compare evaluations

An analysis is carried out to compare the outcomes achieved from four different ML regression models applied to the utilized dataset. The performance metrics for each of these ML methods on the dataset are presented in Table 2. The SVR model achieves a MAPE value of 3.106%, indicating a minimal average deviation between predicted and actual values. Consequently, SVR outperforms the other ML algorithms, demonstrating the lowest MAPE and highest R^2 values. Nevertheless, LR and SGD also exhibit satisfactory performance, while RF emerges as the least efficient ML technique within the scope of this investigation.

Table 2. Compare different metrics for each ML method by considering all features.

Metrics	ML method			
	LR	SVR	RF	SGD
MSE	0.015	0.012	0.024	0.015
MAPE (%)	3.346	3.106	4.238	3.341
R^2	0.866	0.891	0.778	0.866

5. Conclusions

This study's departure from previous literature can be observed, as the study focused on evaluating the compressive strength of hardened AAC samples. Subsequently, four distinct ML estimators—namely SVR, LR, SGD, and RF—were employed to model these measurements. A comparison was drawn between the predicted concrete compressive strength values and their actual counterparts.

SVR demonstrated the most significant performance among the array of ML techniques scrutinized. The model achieved a performance level of 3.106% in terms of MAPE value. This study underscores the efficacy of utilizing ML approaches to facilitate the assessment of AAC block compressive strength, offering advantages in terms of simplicity, speed, and cost-effectiveness.

Scholars could contemplate expanding the dataset to encompass a broader range of parameters and varying conditions to further enhance and progress this research. Exploration of alternative ML methods or the evaluation of their combined effectiveness could also be pursued. Moreover, integrating additional factors, such as curing duration, aggregate quality, and size, could significantly bolster the model's efficacy and yield more comprehensive insights.

By analyzing feature correlations between input parameters and the output (concrete strength), the following conclusions can be drawn:

- Cement and water content are pivotal factors influencing the prediction of concrete strength.
- A notable trend is observed where increased cement content generally corresponds to higher compressive strength. This holds true as long as the mixture maintains proper balance and effective curing procedures. However, it is crucial to acknowledge that there exists a threshold beyond which augmenting cement content might not yield proportionate strength increments. Moreover, there's a possibility of impacting other attributes of the blocks, such as density and insulation capabilities.
- Recognizing the intricate and multifaceted relationship between material proportions and compressive strength is imperative. This connection can vary based on specific manufacturing techniques and formulations. Thus, comprehensive testing and analysis are imperative. Such rigorous assessments are essential for refining material ratios to achieve optimal performance. Preserving other crucial properties inherent to AAC blocks is equally important, including thermal insulation and density.

To sum up, carrying out additional research within the realm of AAC holds both necessity and significance. This effort is pivotal in harnessing the full scope of its advantages, refining construction methodologies, and actively fostering the sustainable progression of the constructed landscape. As ML techniques continue to evolve, the trajectory of AAC block manufacturing appears promising, ushering in a future characterized by heightened safety, enhanced sustainability, and the establishment of resilient and durable structures.

Acknowledgements
None declared.

Funding
The author received no financial support for the research, authorship, and/or publication of this manuscript.

Conflict of Interest
The author declared no potential conflicts of interest with respect to the research, authorship, and/or publication of this manuscript.

Data Availability
The datasets created and/or analyzed during the current study are not publicly available, but are available from the corresponding author upon reasonable request.

REFERENCES

Albuthbahak OM, Hiswa AA (2019). Prediction of concrete compressive strength using supervised machine learning models through ultrasonic pulse velocity and mix parameters. *Revista Romana de Materiale*, 49(2), 232–243.

Aydın Y, Cakiroglu C, Bekdaş G, Işıkdağ Ü, Kim S, Hong J, Geem ZW (2023). Neural network predictive models for alkali-activated concrete carbon emission using metaheuristic optimization algorithms. *Sustainability*, 16(1), 142.

Behnood A, Golafshani EM (2020). Machine learning study of the mechanical properties of concretes containing waste foundry sand. *Construction and Building Materials,* 243, 118152.

Cakiroglu C, Islam K, Bekdaş G, Kim S, Geem ZW (2022). Interpretable machine learning algorithms to predict the axial capacity of FRP-reinforced concrete columns. *Materials*, 15(8), 2742.

Cheng MY, Chou JS, Roy AF, Wu YW (2012). High-performance concrete compressive strength prediction using time-weighted evolutionary

fuzzy support vector machines inference model. *Automation in Construction*, 28, 106–115.

Cohen T, Freytsis M, Ostdiek B (2018). Machine learning to do more with less. *Journal of High Energy Physics*, 2018(2), 1-28.

de Prado-Gil J, Palencia C, Jagadesh P, Martínez-García R (2022). A study on the prediction of compressive strength of self-compacting recycled aggregate concrete utilizing novel computational approaches. *Materials*, 15(15), 5232.

Deshpande N, Londhe S, Kulkarni S (2014). Modeling compressive strength of recycled aggregate concrete by artificial neural network, model tree and non-linear regression. *International Journal of Sustainable Built Environment*, 3(2), 187–198.

DIN 771-4: 2011-07 (2011). Festlegungen für mauersteine–teil 4: Porenbetonsteine. DIN Deutsches Institut für Normung e, V., Berlin, Germany.

DIN 772-1: 2016-05 (2016). Methods of test for masonry units–part 1: Determination of compressive strength. DIN Deutsches Institut für Normung e, V., Berlin, Germany.

Domingo ER (2008). An introduction to autoclaved aerated concrete including design requirements using strength design. Technical report, Kansas State University, Kansas, USA.

Dudukalov E, Munister V, Zolkin A, Losev A, Knishov A (2021). The use of artificial intelligence and information technology for measurements in mechanical engineering and in process automation systems in industry 4.0. In: *Journal of Physics: Conference Series*, Vol. 1889. IOP Publishing, p. 052011.

El-Mir A, El-Zahab S, Sbartaï ZM, Homsi F, Saliba J, El-Hassan H (2023). Machine learning prediction of concrete compressive strength using rebound hammer test. *Journal of Building Engineering*, 64, 105538.

Erdal HI (2013). Two-level and hybrid ensembles of decision trees for high performance concrete compressive strength prediction. *Engineering Applications of Artificial Intelligence*, 26(7), 1689–1697.

Fan Z, Chiong R, Hu Z, Lin Y (2020). A fuzzy weighted relative error support vector machine for reverse prediction of concrete components. *Computers & Structures*, 230, 106171.

Faridmehr I, Nehdi ML, Huseien GF, Baghban MH, Sam ARM, Algaifi HA (2021). Experimental and informational modeling study of sustainable self-compacting geopolymer concrete. *Sustainability*, 13(13), 7444.

Géron A (2017). Hands-on machine learning with scikit-learn and tensorflow: concepts, tools, and techniques to build intelligent systems. O'Reilly Media, Sebastopol, CA, 54–56.

Güçlüer K, Özbeyaz A, Göymen S, Günaydın O (2021). A comparative investigation using machine learning methods for concrete compressive strength estimation. *Materials Today Communications*, 27, 102278.

Hadzima-Nyarko M, Nyarko EK, Ademovic N, Miličević I, Šipoš TK (2019). Modelling the influence of waste rubber on compressive strength of concrete by artificial neural networks. *Materials*, 12(4), 561.

Hamad AJ (2014). Materials, production, properties and application of aerated lightweight concrete. *International Journal of Materials Science and Engineering*, 2(2), 152–157.

Harirchian E, Hosseini SEA, Jadhav K, Kumari V, Rasulzade S, Işık E, Wasif M, Lahmer T (2021). A review on application of soft computing techniques for the rapid visual safety evaluation and damage classification of existing buildings. *Journal of Building Engineering*, 102536.

Harirchian E, Kumari V, Jadhav K, Das RR, Rasulzade S, Lahmer T (2020). *A* machine learning framework for assessing seismic hazard safety of reinforced concrete buildings. *Applied Sciences,* 10(20), 7153.

Islam MM, Hossain MB, Akhtar MN, Moni MA, Hasan KF (2022). CNN based on transfer learning models using data augmentation and transformation for detection of concrete crack. *Algorithms*, 15(8), 287.

Jiang Y, Li H, Zhou Y (2022). Compressive strength prediction of fly ash concrete using machine learning techniques. *Buildings*, 12(5), 690.

Kalpana M, Mohith S (2020). Study on autoclaved aerated concrete. *Materials Today: Proceedings*, 22, 894–896.

Kavita M, Tarjani C (2016). Comparison on auto aerated concrete to normal concrete*. Recent Advances in Civil Engineering for Global Sustainability*, 90–94.

Korotcov A, Tkachenko V, Russo DP, Ekins S (2017). Comparison of deep learning with multiple machine learning methods and metrics using diverse drug discovery data sets*. Molecular Pharmaceutics*, 14(12), 4462-4475.

Krivenko P (2020). Compressive Strength of Concrete. John Wiley & Sons, Inc., Toronto, Canada.

Liu T, Cakiroglu C, Islam K, Wang Z, Nehdi ML (2024). Explainable machine learning model for predicting punching shear strength of FRC flat slabs. *Engineering Structures*, 301, 117276.

Mehmannavaz T, Ismail M, Radin Sumadi S, Rafique Bhutta MA, Samadi M, Sajjadi SM (2014). Binary effect of fly ash and palm oil fuel ash on heat of hydration aerated concrete. *The Scientific World Journal*, 2014.

Muhammad W, Brahme AP, Ibragimova O, Kang J, Inal K (2021). A machine learning framework to predict local strain distribution and the evolution of plastic anisotropy & fracture in additively manufactured alloys. *International Journal of Plasticity*, 136, 102867.

Mylvaganam N, Elakneswaran Y (2023). A systematic review and assessment of concrete strength prediction models. *Case Studies in Construction Materials*, e01830.

Narayanan N, Ramamurthy K (2000). Structure and properties of aerated concrete: a review. *Cement and Concrete Composites*, 22(5), 321–329.

Ni HG, Wang JZ (2000). Prediction of compressive strength of concrete by neural networks. *Cement and Concrete Research,* 30(8), 1245–1250.

Qu X, Zhao X (2017). Previous and present investigations on the components, microstructure and main properties of autoclaved aerated concrete–a review. *Construction and Building Materials*, 135, 505–516.

Rafiza AR, Fazlizan A, Thongtha A, Asim N, Noorashikin MS (2022). The physical and mechanical properties of autoclaved aerated concrete (AAC) with recycled AAC as a partial replacement for sand. *Buildings*, 12(1), 60.

Ramamurthy K, Nambiar EK, Ranjani GIS (2009). A classification of studies on properties of foam concrete. *Cement and Concrete Composites*, 31(6), 388–396.

Różycka A, Kotwica L (2022). Waste originating from the cleaning of flue gases from the combustion of industrial wastes as a lime partial replacement in autoclaved aerated concrete*. Materials*, 15(7), 2576.

Schober G (2011). Porosity in Autoclaved Aerated Concrete (AAC): A review on pore structure, types of porosity, measurement methods and effects of porosity on properties. *Proceedings of the 5th International Conference on Autoclaved Aerated Concrete*, Bydgoscsz, Poland, 351–359.

Shah HA, Yuan Q, Akmal U, Shah SA, Salmi A, Awad YA, Shah LA, Iftikhar Y, Javed MH, Khan MI (2022). Application of machine learning techniques for predicting compressive, splitting tensile, and flexural strengths of concrete with metakaolin. *Materials*, 15(15), 5435.

Tosee SVR, Faridmehr I, Bedon C, Sadowski L, Aalimahmoody N, Nikoo M, Nowobilski T (2021). Metaheuristic prediction of the compressive strength of environmentally friendly concrete modified with eggshell powder using the hybrid ANN-SFL optimization algorithm. *Materials*, 14(20), 6172.

Wongkeo W, Thongsanitgarn P, Pimraksa K, Chaipanich A (2012). Compressive strength, flexural strength and thermal conductivity of autoclaved concrete block made using bottom ash as cement replacement materials. *Materials & Design*, 35, 434–439.

Yang Q, Du S (2015). Prediction of concrete cubic compressive strength using ANN based size effect model. *Computers, Materials & Continua*, 47(3).